Computer Methods and Programs in Biomedicine 273 (2026) 109116

Contents lists available at ScienceDirect

Computer Methods and Programs in Biomedicine

journal homepage: https://www.sciencedirect.com/journal/computer-methods-and-programs-in-biomedicine

Exploring design strategies for patient-specific bone scaffolds to create a uniform mechanical environment in trabecular bone

Andrea Fresquet-Monter *, Ricardo Belda, Ana Vercher-Martínez, Raquel Megías, Eugenio Giner

Institute of Mechanical Engineering and Biomechanics- I2MB, Department of Mechanical Engineering and Materials, Universitat Politècnica de València, Camino de Vera, s/n, Valencia, 46022, Spain

ARTICLE INFO

Keywords:
Triply Periodic Minimal Surface structures
Patient-specific bone scaffolds
Finite element method
Morphometric characterisation
Load bearing
Trabecular bone

ABSTRACT

Background and Objective: Large bone defects cannot be repaired by the inherent regeneration mechanisms of bone due to their size, which makes medical intervention essential. Current therapeutic treatments have their limitations, which has led to the study and development of bone scaffolds that maintain structural integrity during bone healing. Novel designs are required to create a mechanical environment that promote osseointegration. In this work, we aim to analyse the effect of patient-specific designs on the creation of a uniform mechanical environment in bone-scaffold constructs.

Methods: Novel patient-specific Triply Periodic Minimal Surface (TPMS) structures were designed according to the characterisation of the microstructure of healthy and osteoporotic human cancellous bone to mimic morphometry. In addition, the assessment of the TPMS representative volume element size was also considered for scaffold design. The interaction between bone and scaffold was analysed through finite element model simulation. In those bone-scaffold assemblies we evaluated three different design strategies: (1) matching bone microstructure; (2) similar apparent compression elastic modulus; and (3) mimicking both the morphometry and the apparent modulus of trabecular bone.

Results: The stress distribution in patient-specific TPMS scaffolds is 83.86 % similar to that of the targeted bone, significantly outperforming the 54.41 % similarity of non-patient-specific solutions.

Conclusions: The design of novel patient-specific scaffolds based on a microstructure similar to cancellous bone allows a uniform stress distribution. Hence, matching both the bone morphometry and apparent elastic modulus is a key issue to reducing stress shielding phenomena and inducing osseointegration.

1. Introduction

Large bone defects are mainly caused by high-energy trauma, tumour resections, infections, or previous fractures (i.e. osteoporosis) [1]. These defects are characterised by a size larger than 2 cm in length and a bone loss of more than 50% in the surrounding tissue, which prevents bone from combating against their critical size with its self-regeneration and self-repair mechanisms. Therefore, such defects are unlikely to heal without intervention [2]. Among current therapeutic strategies, there are external and internal fixation systems, such as bone or intramedullary screws [3]. However, the great drawback of these systems is that they are not adapted to the porous and curved structure of bone, resulting in a higher incidence of complications during and after surgery [3]. Furthermore, since they are rigid and solid, they have unfavourable mechanical properties for the adjacent bone tissue [3].

Consequently, the gold standard treatment for large bone defects and fractures is bone grafts, which are structural implants with the capacity to induce osteoinductive, osteoconductive, and osteogenic processes [1,4]. Bone grafts are classified into three types: autografts (from the own patient), allografts (from another human donor), and xenografts (derived from an animal), although autografts are deemed as the clinical standard reconstruction technique [4,5]. Nevertheless, these grafts also present several disadvantages: the bone volume required to treat these defects, the patient's underlying pain due to the extraction of bone tissue, and the risk of infection, leading to graft resorption that prevents bone union [6]. In the case of allografts, they have been associated with immunogenic responses and risk of disease transmission, while xenogeneic grafts are involved in the transmission of zoonotic diseases and immune rejection, in addition to the ethical concerns they entail [1]. Moreover, it is also worth mentioning that

* Corresponding author.
E-mail address: afremon@upv.es (A. Fresquet-Monter).

https://doi.org/10.1016/j.cmpb.2025.109116
Received 15 June 2025; Received in revised form 19 September 2025; Accepted 8 October 2025
Available online 13 October 2025

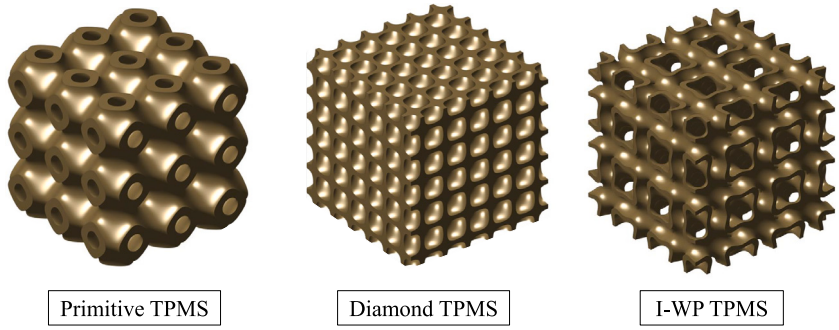

Fig. 1. Primitive, diamond and I-WP TPMS structures.

the vast majority of clinical grafts fail due to incorrect vascularisation, which decreases the exchange of nutrients, gasses and waste between the graft and tissue, leading to the necrosis of the graft [1].

Therefore, due to the limits of the aforementioned therapies, synthetic bone substitutes are being developed and studied by bone tissue engineering [7,8]. These scaffolds have the same function as bone grafts: they fill the gaps of bone defects and provide an adequate mechanical strength and environment for cell proliferation, migration, differentiation, and mineralisation during bone remodelling [7]. To that end, synthetic bone substitutes must meet the following requirements: being biocompatible in order to promote cell attachment and proliferation, being biodegradable to guarantee the replacement of the scaffold with regenerated tissue, having enough mechanical strength, and possessing a porous microstructure to mimic the native extracellular matrix [7]. Several techniques are used to manufacture these scaffolds, such as electrospinning, phase separation, or gas foaming, among others [7]. However, these methods are limited to 2D or very simple 3D structures, which do not have the capacity to produce more complex geometries [7]. Therefore, additive manufacturing techniques (also called 3D printing) are a great solution for this limitation because they are cost-effective and allow the design of complex structures with a variety of materials [7]. Additionally, it is worth mentioning that 3D printing also permits the manufacture of custom bone scaffolds, thereby producing bone substitutes for specific bone defects [3].

Among bone scaffolds, porous structures have gained great relevance due to their exceptional mechanical performance: high stiffness, load transmission capacity, and energy absorption [9]. Consequently, the biomedical scientific community is focused on studying and using these porous scaffolds as bone substitutes owing to the high ongoing and future increase in both large bone fractures and defects [9,10]. With the current development and progress in additive manufacturing, great candidates for bone substitution have emerged: Triply Periodic Minimal Surface (TPMS) structures [11]. TPMS scaffolds present several advantages, such as their versatile architecture, which makes it possible to control the geometry and pore size of the scaffold, their zero-mean curvature at any point on their surface, their lower level of stress concentrators, which leads to a more uniform load transmission, and their high surface area and pore interconnectivity, crucial for cell adhesion and growth [11,12]. Furthermore, it has been observed that TPMS structures may have a microarchitecture similar to trabecular bone, so that they can integrate well with the surrounding tissue and promote cellular processes such as oxygen diffusion, ion exchange and nutrient transport, essential mechanisms for cell differentiation and proliferation [9,11]. In Fig. 1 the conventional architectures of primitive, diamond and I-graph-wrapped package (I-WP) TPMS structures are shown.

In literature, numerous studies have reported correlations between the design and the mechanical and permeability properties of TPMS scaffolds. An investigation carried out by Verma et al. (2022) [13] evaluated the mechanical characteristics of Ti6Al4V gyroid and primitive porous TPMS scaffolds and established a relation between geometry dimension, porosity, and stiffness, indicating that porosity could decrease stiffness in such scaffolds. Peng et al. (2023) [14] designed gyroid structures with hollow-struts to control both the mechanical and permeability characteristics of these scaffolds. Their results showed that changing the volume fraction and the volume ratio of the inner pore allowed tuning the mechanical properties and mass-transport capacity of the scaffolds. The TPMS morphology also plays an important role in the deformation mechanisms. Hence, Maskery et al. (2018) [15] found that the deformation process of primitive TPMS scaffolds was ruled by strut stretching and buckling, while gyroid and diamond designs were dominated by bending deformations. Regarding the biomechanical performance of TPMS scaffolds, Maevskaia et al. (2023) [16] produced hydroxyapatite-based gyroid, diamond, and primitive scaffolds and observed that gyroid and diamond designs showed higher compression strengths and bone ingrowth *in vivo*. Consequently, the variation of the architectural parameters of TPMS structures results in different mechanical strengths and permeabilities, which in turn affect the rate of bone regeneration and the mechanical performance of the scaffold [10,11]. However, the analysis of stress transfer between bone and TPMS scaffold using patient-specific designs has not yet been evaluated in detail. The required mechanical performance of the scaffolds greatly depends on bone type as well as patient's age and gender and adjusting the microstructural characteristics of scaffolds to those specific to bone can be a solution [17–19]. At the same time, it is important for the primary fixation of a bone substitute that the scaffold matches the mechanical properties and local loading conditions of the target bone [19]. This is decisive when designing bone scaffolds to avoid stress shielding phenomena and allow the integration of the bone substitute into the tissue, achieving long-term osseointegration [20]

In this study, we demonstrate, through numerical simulations, that a patient-specific scaffold design creates a stable mechanical environment. Specifically, our objective is to analyse the differences in load bearing in bone-scaffold constructs that have an apparent elastic modulus and a morphometry similar or different from trabecular bone, thus observing the effect of these two characteristics on stress transfer. To that end, we followed three different design strategies for the assemblies: first, constructs with TPMS scaffolds that match bone microstructure; second, assemblies with TPMS structures that have an apparent compression modulus similar to cancellous bone; and third, constructs with TPMS scaffolds that mimic both the morphometry and the apparent modulus of trabecular bone.

Following this introduction, the present work is organised as follows: in Section 2 we provide a brief description of the methodology followed in this work. This includes the morphometric characterisation of human cancellous bone samples and the design, manufacturing, and assessment of the mechanical properties of TPMS scaffolds. In addition, we describe the design procedure and numerical analysis of bone-scaffold assemblies. Then, in Section 3 we present the results of this study. Lastly, in Sections 4 and 5 the discussion and conclusions of this work are given, respectively.

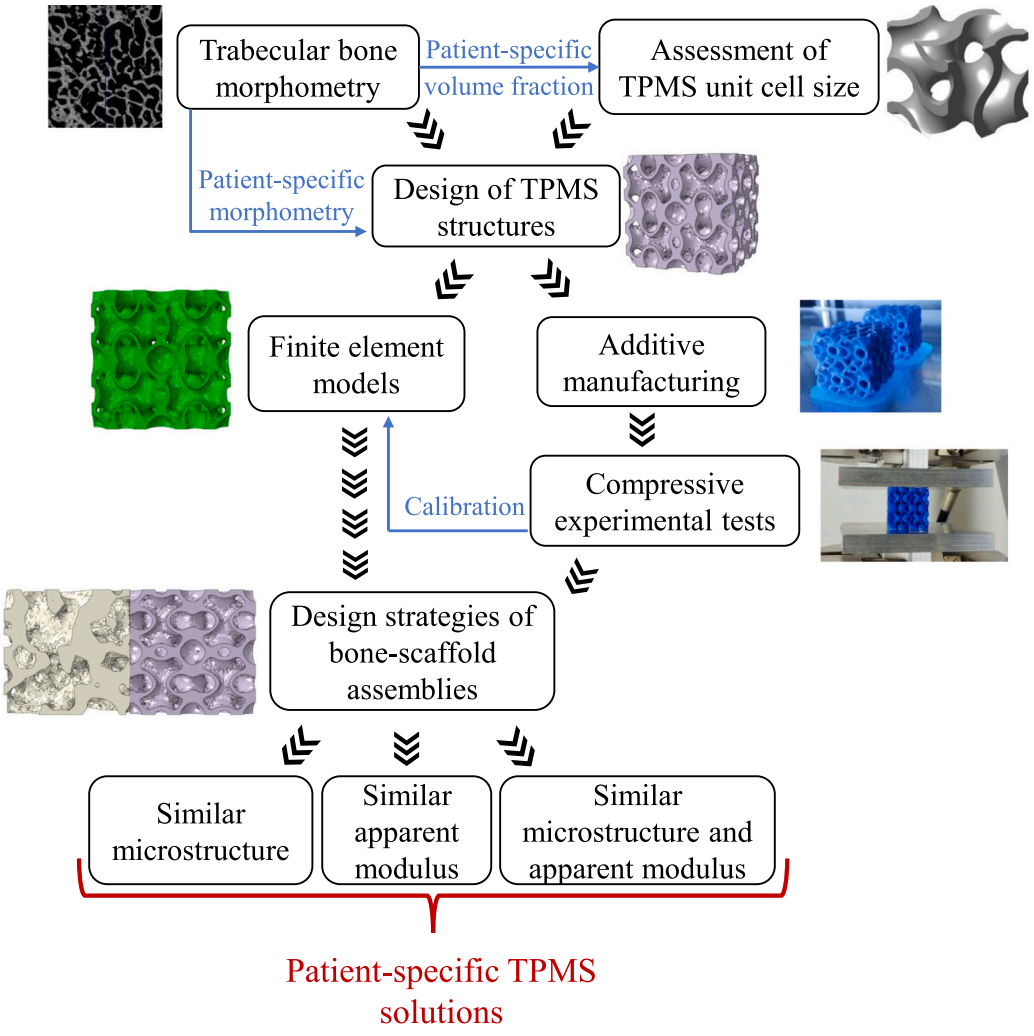

Fig. 2. Methodology followed during this study.

2. Materials and methods

In this work, we have followed a methodology that includes the design of TPMS representative volume elements (RVEs), prototype manufacturing, compression testing, and numerical modelling, as depicted in Fig. 2. The design of patient-specific solutions involves both the characterisation of cancellous bone samples from osteoporotic and healthy donors and the dimension analysis of TPMS RVEs. Then, we design new scaffolds and evaluate the influence of the volume fraction on the morphometry and mechanical response. Lastly, the interaction between bone and scaffold is evaluated through finite element model simulation, bearing in mind the three aforementioned bone-scaffold assembly design strategies.

2.1. Cancellous bone sample description and imaging

To evaluate the influence of patient-specific bone substitutes on the mechanical response of bone-scaffold assemblies, we first analysed two cancellous bone specimens. Those were obtained from human femoral heads extracted during total hip arthroplasty surgery at the Hospital Universitario Infanta Leonor of Madrid. The samples chosen for this study belonged to healthy and osteoporotic bones.

The parallelepiped specimens were cut from the femoral heads using a Microtom Struers precision saw (Struers, Denmark). To remove organic remains, the samples were subjected to ultrasound baths in distilled water. To characterise the 3D bone microarchitecture, the cancellous bone samples were scanned using micro-CT (Skyscan1172 (Bruker, Belgium)) at the Estación de Bioloxía Mariña at A Graña (University of Santiago de Compostela) achieving an isotropic resolution of 13.5 μm (voltage 100 kV, intensity 100 μA, Al/Cu filter).

The micro-CT images were segmented using a global thresholding method. From the resulting bone mask, a 3 mm cubic region of interest (ROI) was selected to generate bone-scaffold constructs to evaluate patient-specific designs. The mechanical properties of the complete samples were characterised using finite element models combined with experimental compression tests [21]. On the one hand, quasi-static compression tests were conducted using a displacement control at a speed of 1 mm/min with the electromechanical testing machine MTS Criterion C42 (MTS Systems, USA). A contact deflectometer (MTS ref. 632.06H-20) was used to measure the displacement between the two compression platens. During the compression test, we recorded the displacement u using the deflectometer and the applied force F employing the load cell of the testing machine. From the registered response, we obtained the stress–strain curves, which allowed the estimation of the apparent modulus $E_{app,exp}$ in each orthogonal direction. FE models were generated from the micro-CT images, obtaining the microstructure of the cancellous specimens. We defined the behaviour of trabecular bone as homogeneous, isotropic, and linear-elastic. An inverse analysis was conducted to estimate the elastic properties. We inferred the values for the estimated parameters and made several iterations until the numerical response matched the experimental stress–strain curve. To calibrate the Young's modulus at the tissue level, we captured the

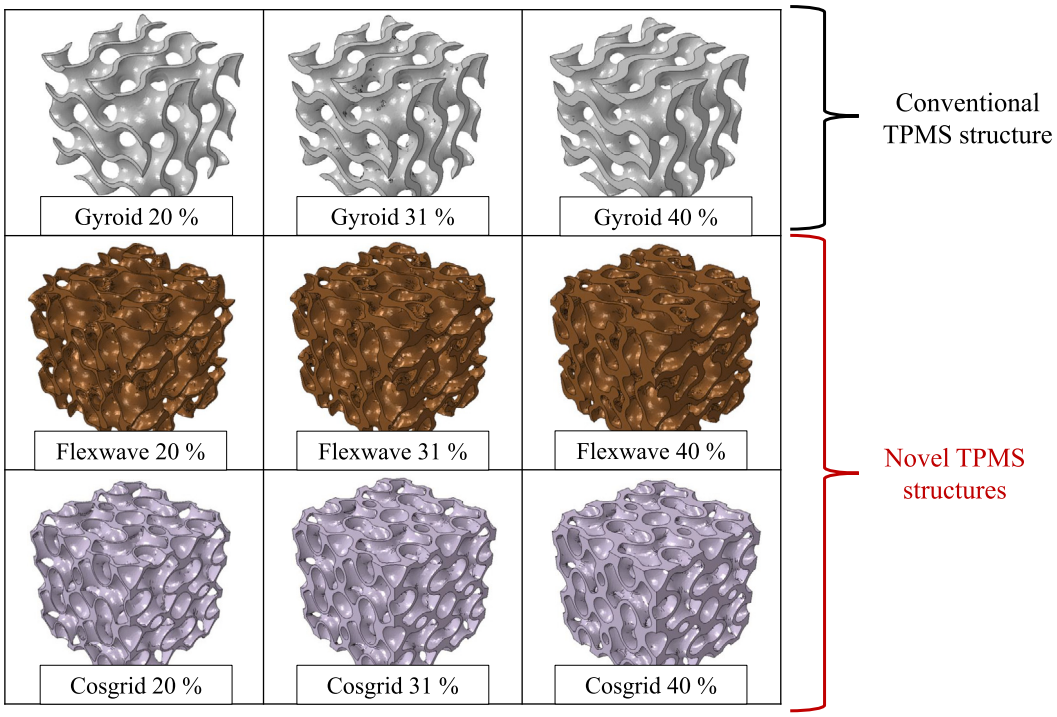

Fig. 3. TPMS scaffold designs considered during this study.

response in the elastic range of the stress–strain compression curve. The elastic modulus of both trabecular specimens was 11.82 GPa for the healthy bone sample and 14.77 GPa for the osteoporotic cancellous tissue [21].

2.2. New design strategies with TPMS structures

In this study, we have analysed various design strategies for TPMS-based bone scaffolds, with the aim of adapting them to patient-specific bone architecture. To overcome the loss of uniformity in load transmission in the bone-scaffold system, we focused on replicating the bone stiffness and reducing stress concentrators.

Several TPMS structures are known, but gyroid, diamond, and primitive are the most frequently studied geometries for tissue-engineered bone substitutes [16]. Among them, the gyroid is the most popular for its excellent mechanical performance and, compared to other TPMS geometries, its high permeability and stiffness, which are essential for cell adhesion and a stable mechanical environment [16,22,23]. In addition, gyroid topology has been shown to have a higher precision in manufacturing than other porous scaffolds, such as the Schwarz diamond structure [24]. Therefore, a gyroid topology was selected in this study (see Eq. (1)). On the other hand, we combined the mathematical functions of gyroid, diamond, primitive, and I-WP structures in order to develop two new in-house geometries and study the following design features. Firstly, we introduced high-frequency terms to replicate the highly tortuous architecture of aged or osteoporotic bone [25,26], with the aim of mimicking the apparent and local bone stiffness. The new design was denoted as Flexwave due to its adaptability and curvature variation that contribute to reducing the load field discontinuity. Secondly, we explored the potential benefits of increasing structural uniformity by designing Cosgrid, which is based on a smooth cosine trigonometric architecture. These geometries are expressed in Eqs. (2) and (3).

$$Gyroid(x,y,z) : \cos(2\pi x)\cdot\sin(2\pi y)+\cos(2\pi y)\cdot sin(2\pi z) + \cos(2\pi z)\cdot sin(2\pi x) = C \quad (1)$$

$$Flexwave(x,y,z) : \cos(4\pi y)\cdot\sin(4\pi z)+\cos(4\pi x)\cdot\sin(4\pi y)+\cos(4\pi z)\cdot\sin(4\pi x)+ \sin(2\pi x)\cdot sin(2\pi y)+\sin(2\pi z)\cdot\sin(2\pi y)+\sin(2\pi z)\cdot\sin(2\pi x)-\cos(2\pi x)\cdot\cos(2\pi y)+ \cos(2\pi z)\cdot\cos(2\pi y)+\cos(2\pi z)\cdot\cos(2\pi x) = C \quad (2)$$

$$Cosgrid(x,y,z) : \cos(4\pi x)\cdot\cos(2\pi z)+\cos(4\pi y)\cdot\cos(2\pi x)+\cos(4\pi z)\cdot\cos(2\pi y) = C \quad (3)$$

The range of bone volume fraction (BV/TV) of the femoral trabecular tissue oscillates between 11.8% and 48.1% according to Hildebrand et al. (2009) [27]. As a consequence, we decided to design TPMS structures with relative densities in that range in order to assess the effect of volume fraction on both the morphometry and mechanical properties of TPMS scaffolds. The selected relative densities were: 20%, 31%, and 40% (note that 31% corresponds to the patient-specific volume fraction of the healthy specimen analysed in this study). In total, we designed 9 TPMS structures (gyroid, Flexwave, and Cosgrid) with the freely available design software MSLattice [28], as shown in Fig. 3.

2.3. Morphometric characterisation

The microstructure of trabecular bone has been shown to greatly impact its mechanical behaviour [29]. Therefore, it is crucial to study cancellous morphometry in order to design bone scaffolds accordingly.

For the purpose of characterising the microstructure of cancellous specimens, we first segmented the micro-CT images corresponding to the healthy and osteoporotic trabecular samples using the software ScanIP (Simpleware, UK) by means of combining a manual thresholding method with a connectivity analysis. Consequently, groups of voxels not connected to the main cancellous structure were removed, which otherwise could cause numerical problems in the simulations. The 3D reconstruction of the healthy and osteoporotic cancellous bone specimens is depicted in Fig. 4. Then, we analysed the morphometry of both

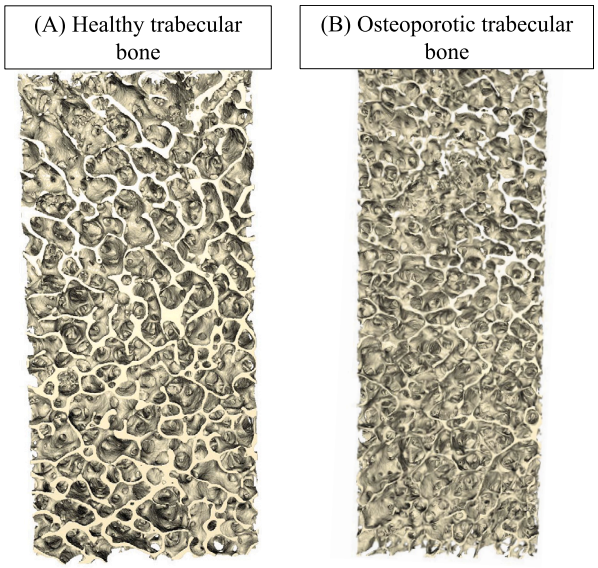

Fig. 4. 3D reconstruction of both trabecular samples. (A) Healthy cancellous specimen obtained from a femoral head from a 43-year-old woman. (B) Osteoporotic trabecular specimen obtained from a femoral head from a 70-year-old man.

segmented images with BoneJ (ImageJ, USA), estimating the following microstructural parameters: bone volume fraction (BV/TV), bone surface per total bone volume (BS/BV), mean trabecular thickness (Tb.Th), mean trabecular separation (Tb.Sp), number of trabeculae (Tb.N), fractal dimension (D), and the degree of anisotropy (DA), which are parameters commonly evaluated in the morphometric characterisation of cancellous tissue [27,30,31].

In the case of TPMS bone scaffolds, we followed a very similar procedure. Once the TPMS scaffolds were designed, solid models of each structure were developed with the software ScanIP. That modelling consisted of obtaining a 3D solid mask of each TPMS structure by filling the cavities of its superficial mask and then analysing the connectivity of the TPMS scaffold in order to once again remove disconnected pixels from the main structure. Lastly, we estimated with BoneJ the aforementioned morphometric parameters.

2.4. Assessment of TPMS representative volume element size

The morphometry and 3D printing of TPMS structures have been shown to depend on both the geometry and the size of their representative volume elements [32]. On that account, in this section we explored the relation between the RVE size and the TPMS microstructure in order to define RVE dimensions according to the morphometry of cancellous bone, thus elucidating which RVE size matched the microstructural characteristics of trabecular bone.

To this end, we designed five different TPMS scaffolds for each type of geometry, all with the patient-specific volume fraction of 31%. Each design had a total size of $3 \times 3 \times 3$ mm, but each of them was composed of a different number of RVEs and, consequently, distinct RVE sizes. As shown in Fig. 5, we designed TPMS structures with one, two, three, four, and five RVEs per direction, which corresponded to RVEs of 3 mm, 1.5 mm, 1 mm, 0.75 mm, and 0.6 mm size, respectively.

2.5. Assessment of the mechanical properties of novel bone scaffolds based on TPMS structures and patient-specific morphometric parameters

2.5.1. Scaffold manufacturing by 3D-printing

Bearing in mind that the volume fraction of TPMS structures remains constant for RVE size variation [12], we escalated by 10 the size of the RVEs in order to detail with more precision the morphometry of the printed scaffolds. Therefore, the size of the TPMS structures was $30 \times 30 \times 30$ mm.

The scaffolds were manufactured by fused deposition modelling, specifically by applying the extrusion-based 3D printing technique using polylactic acid (PLA) filament with a BCN3D Epsilon W50 printer (BCN3D, Spain) (see Fig. 6). Four samples of each volume fraction of each TPMS structure were printed in order to evaluate the repeatability of scaffold fabrication. The STL files were imported into the BCN3D Stratos software (v1.6.3.) to set the printing parameters. The printing conditions were set as follows: nozzle diameter of 0.4 mm, infill of 100%, layer thickness of 0.15 mm, without support, extruder head temperature of 210 °C, print speed of 60 mm/s, bed temperature of 45 °C, and a brim-type adhesion to the plate. Later, the TPMS structures were studied using an Xradia 620 versa (Zeiss, Germany) high resolution computed tomography scanner at the Universitat Politècnica de València in order to examine the internal architecture of the manufactured structures and assess their printing quality (resolution = 45.5 μm, voltage = 30 kV, and exposure time = 25 s).

2.5.2. Experimental characterisation of TPMS scaffolds

The compression tests were conducted with the electromechanical testing machine MTS Criterion C42. Three samples were tested for each TPMS geometry and volume fraction. The structures were placed parallel to the compression platens in order to minimise shear stresses during the tests. The quasi-static compression tests were carried out using a displacement control at a constant speed of 5 mm/min. A contact deflectometer was used to measure the displacement between both compression platens as shown in Fig. 7. Before the tests, we applied a 10 N preload. During the test, we recorded the displacement u using the deflectometer and the applied force F by the load cell of the testing machine. From the registered response, stress–strain graphs were obtained, which allowed us to estimate the apparent compression elastic modulus ($E_{app,exp}$) of each TPMS scaffold.

2.5.3. Numerical analysis of TPMS scaffolds

After conducting a mesh sensitivity study to determine the element size, we proceeded to create finite element (FE) models of the 9 TPMS scaffolds, with the purpose of replicating the microstructure of each lattice sample (see Fig. 8). FE meshes were generated using the software ScanIP and then modelled with quadratic tetrahedral elements (C3D10 in Abaqus), resulting in a mesh of 771k ± 323k nodes and a mean element size of 0.75 ± 0.21 mm. Using Abaqus Standard (v6.14, Dassault Systems, USA), we defined the following boundary conditions: a displacement of 1% of the length of the TPMS structure was applied to one surface, while the displacement on the opposite surface was restricted in all directions.

We considered the behaviour of triply periodic lattice structures at the strut level to be homogeneous, isotropic, and linear-elastic, for that enabled us to estimate the apparent modulus $E_{app,num}$ of each TPMS scaffold. An initial Young's modulus E of 10 GPa and a Poisson's ratio ν of 0.3 were defined at the material level. Lastly, by calibrating the elastic response of the numerical results with the experimental tests, the Young's modulus of the printing material (PLA) was inferred.

2.6. Generation of bone-scaffold assemblies according to the patient-specific strategy designs

The last step of this study consisted of analysing the apparent Young's modulus and stress distribution of bone-scaffold assemblies, with the purpose of evaluating the effect of a morphometry and/or apparent elastic modulus similar to cancellous bone on load transfer between both structures.

Consequently, we first cut out a random fragment of 3 mm size of both the osteoporotic and healthy trabecular bone sample, which later were morphometrically and numerically characterised. The tortuous

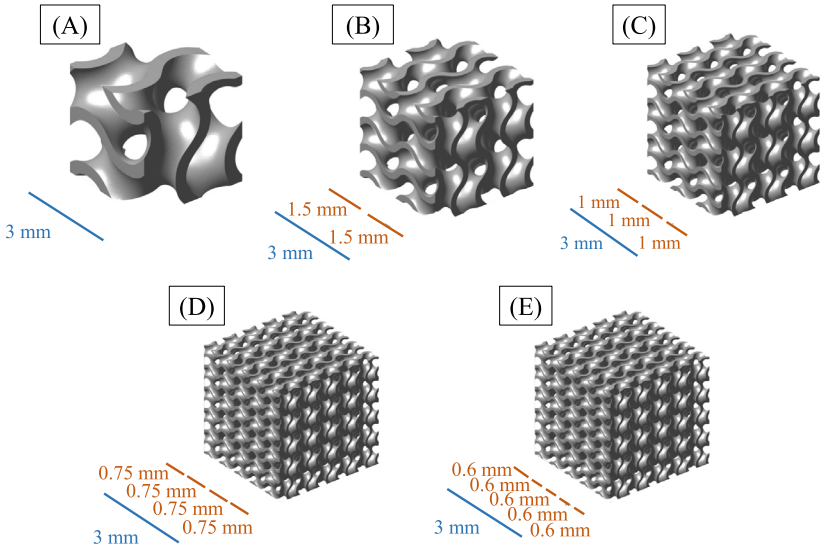

Fig. 5. Designs of the five gyroid TPMS structures with different RVE sizes. In blue the total size of the TPMS structures is indicated, while in orange the size of the TPMS RVEs is specified. (A) One RVE of 3 mm per direction. (B) Two RVEs of 1.5 mm each per direction. (C) Three RVEs of 1 mm each per direction. (D) Four RVEs of 0.75 mm each per direction. (E) Five RVEs of 0.6 mm per direction.

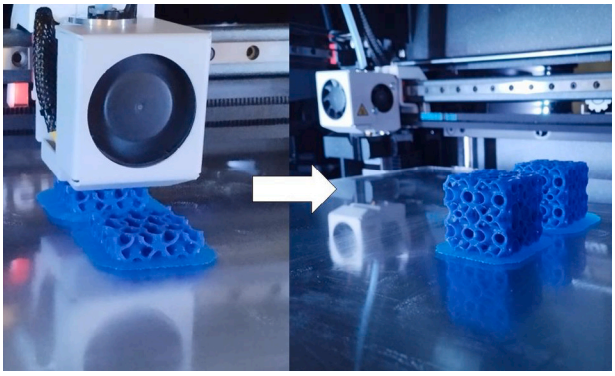

Fig. 6. Manufacture of Cosgrid TPMS structures with a volume fraction of 40%.

and complex microarchitecture of bone and the TPMS scaffold resulted in an unstable surface contact between the two structures when trying to implement a surface-to-surface contact or general contact in Abaqus, which led to model convergence problems. In this way, all bone-scaffold constructs were generated in ScanIP by placing the bone on top of the scaffold, so a material transition occurred at the interface between both structures. This does not exactly represent the interaction between bone and scaffold and therefore does not accurately reflect the mechanical behaviour of the construct. Then, we generated the models of each construct with ScanIP and analysed them numerically with the same procedure as stated in Section 2.5.3 using Abaqus. It is worth mentioning that the displacement was applied to the cancellous bone surface in the compression direction, which corresponded to the X axis, for in both healthy and osteoporotic trabecular bone specimens that was the stiffest direction. Meanwhile, the scaffold surface was restrained in all directions. The specified boundary conditions are indicated in Fig. 9.

That way, we designed bone-scaffold constructs with different morphometric and mechanical characteristics with the purpose of assessing three different design strategies. First, we studied the influence of considering a morphometry similar to or different from trabecular bone on the distribution of mechanical stresses between both structures. On that account, bone-scaffold assemblies were composed of Flexwave surrogates with the patient-specific relative densities of 20%, 31% and 40% using two different materials. Second, considering a metallic alloy for the porous TPMS scaffolds, which is common in clinical implants, we designed TPMS scaffolds with apparent mechanical properties similar to healthy and osteoporotic trabecular bone. That was accomplished by reducing the volume fraction of the Flexwave TPMS structure until we obtained an apparent elastic modulus similar to the trabecular bone sections. Third, we designed bone-scaffold assemblies with both a morphometry and an apparent modulus similar to trabecular bone by considering patient-specific TPMS solutions and a material's Young's modulus close to cancellous tissue. The Flexwave TPMS structure with different volume fractions was taken into account for the first two approaches, whereas all patient-specific TPMS surrogates were considered for the construction of bone-scaffold assemblies in the third design strategy. This is summarised in Table 1.

To qualitatively assess the stress transmission between the bone and TPMS scaffold in the assemblies, we represented their principal stresses in the compression direction with a colour map. In addition, we quantitatively evaluated the load bearing by analysing the histograms of those same stresses. This novel procedure aims to compare the histogram stresses of the scaffold and bone, thus evaluating the hypothesis that a patient-specific design creates a uniform mechanical environment that promotes bone formation. The objective of this comparison is that the scaffold matches the mechanical behaviour of bone. Therefore, we consider bone as the ground truth. Once the histograms were visualised, we obtained the binary segmented mask of each histogram and estimated the Jaccard index (J) using Eq. (4) in order to quantify the similarity between both stress distributions. The estimation of this coefficient is common for the quality evaluation of a segmentation procedure [33]. The Jaccard index relates the true positive (TP) with the sum of true positive, false positive (FP), and false negative (FN). TP is defined as the scaffold mask that matches the one of the bone, FP represents the stresses in the scaffold histogram that do not match the one of the bone, and FN refers to the bone stresses in the histogram mask that are not included in the one of the scaffold. A high Jaccard coefficient suggests a great similarity between both segmentations, whereas a low value represents a significant difference.

$$J = \frac{TP}{TP + FP + FN} \tag{4}$$

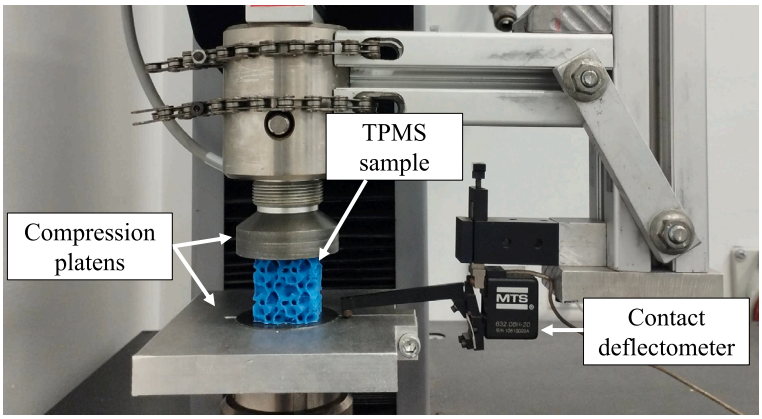

Fig. 7. Experimental setup used for conducting the compression tests.

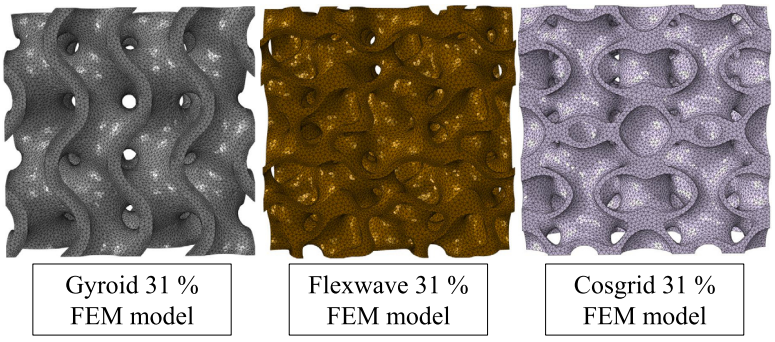

Fig. 8. Finite element models of the three TPMS structures analysed in this work with a volume fraction of 31%.

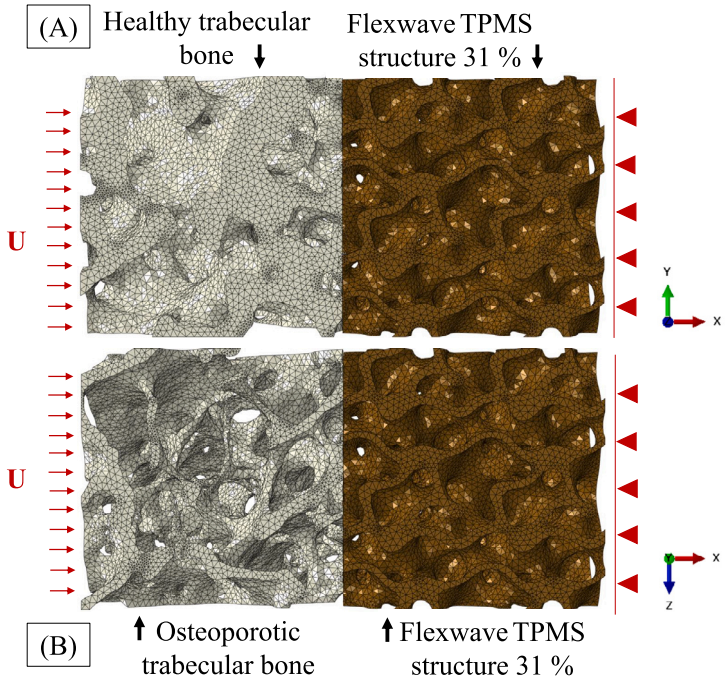

Fig. 9. Boundary conditions of healthy (A) and osteoporotic (B) assemblies with Flexwave considering a volume fraction of 31%.

Table 1
TPMS structures considered for bone-scaffold assemblies in each design strategy.

TPMS scaffold	1st design strategy: Similar microstructure	2nd design strategy: Similar $E_{app,num}$	3rd design strategy: Similar microstructure and $E_{app,num}$
Gyroid-20%	–	–	✓
Gyroid-31%	–	–	✓
Gyroid-40%	–	–	✓
Flexwave-6.2%	–	✓	–
Flexwave-12%	–	✓	–
Flexwave-20%	✓	–	✓
Flexwave-31%	✓	–	✓
Flexwave-40%	✓	–	✓
Cosgrid-20%	–	–	✓
Cosgrid-31%	–	–	✓
Cosgrid-40%	–	–	✓

Table 2
Morphometric characterisation of healthy and osteoporotic trabecular bone.

Morphometric characteristic	Healthy trabecular specimen	Osteoporotic trabecular specimen
BV/TV [%]	30.63	16.379
BS/BV [mm^{-1}]	13.092	19.750
Tb.Th [mm]	0.241	0.166
Tb.Sp [mm]	0.658	0.953
Tb.N [mm^{-1}]	1.270	0.988
DA [–]	0.216	0.231
D [–]	2.519	2.466
Conn.D [mm^{-3}]	$1.862 \cdot 10^{-7}$	$3.170 \cdot 10^{-11}$

3. Results

3.1. Morphometric characterisation of trabecular bone

The morphometric characterisation of cancellous bone allowed us to observe the effects of osteoporosis on bone microstructure and to define patient-specific scaffold designs according to bone morphometry (see Table 2). The results show that a decrease in volume fraction is due to bone loss, since the relative density of the pathological tissue (16.38%) is half of the healthy specimen (30.63%). This also implies a reduction in Tb.Th and Tb.N in the case of the osteoporotic bone. In contrast, there is an increase in porosity in the pathological tissue that may increment Tb.Sp (0.953 mm in the osteoporotic case compared to 0.658 mm in healthy bone). Lastly, we also observe a decrease in connectivity density in the osteoporotic tissue.

Therefore, the patient-specific volume fraction of 30.63% from healthy bone was taken into account for the evaluation of TPMS RVE size. On the other hand, for the design of TPMS scaffolds, the patient-specific relative densities of both healthy and osteoporotic trabecular bone (30.63% and 16.38%, respectively) were also considered.

3.2. Optimal range of RVE size for patient-specific TPMS scaffolds

By keeping the volume fraction constant to 31% and varying the RVE size in the TPMS scaffolds, we obtained the results summarised in Table 3 for the Flexwave structure (the results from Cosgrid and Gyroid can be found in Tables A.1 and A.2, respectively). The dimension analysis of the different structures shows that the reduction of RVE size leads to a higher $TPMS_S/TPMS_V$, which indicates a larger surface area, beneficial for the exchange of nutrients and waste. It also suggests a decrease in both the mean strut thickness and mean strut separation but an increment in the number of struts. Moreover, the fractal dimension increases slightly when reducing the RVE size, possibly due to an increase in the complexity of the TPMS structure. The opposite occurs with Conn.D, which becomes larger when increasing the RVE size. Lastly, the value of anisotropy degree is in the five cases very similar and close to 0 regardless of the RVE size, indicating the isotropic behaviour of TPMS scaffolds owing to their triple periodicity.

Once the relation between the microstructural characteristics and the RVE size was elucidated, we proceeded to compare the morphometric results from the 3 TPMS scaffolds with the normal morphometric range of cancellous bone tissue from human femoral heads collected by Hildebrand et al. (2009) [27]. This comparison reveals that an RVE size approximately from 1.5 mm to 3 mm, approximately because it depends on which microstructural characteristic and TPMS geometry we are observing, satisfies the requirements of bone morphometry. Specifically, this range allows mimicking bone surface area, mean trabecular thickness and separation, and number of trabeculae when considering a volume fraction of 31%, as shown in Fig. 10. Thus, for the design of all TPMS structures in this study, we chose an RVE size of 1.5 mm.

3.3. Effect of patient-specificity on the microstructural and mechanical performance of TPMS scaffolds

The morphometric results of all 9 TPMS structures can be found in Table 4. They show that an increase in volume fraction results in a decrease in both strut surface area and mean strut separation, but an increment in strut thickness as well as in the number of struts. Furthermore, by comparing again these results with the morphometric ranges of trabecular bone tissue [27], we see that the gyroid, Flexwave and Cosgrid TPMS structures with volume fractions of 31% and 40% match the microstructural characteristics of healthy cancellous bone, something we hypothesise to be essential for the design of patient-specific bone scaffolds.

A relative error below 8% in pore size and volume fraction was found in all scaffolds printed with a relative density of 31% and 40%, indicating a morphometry close to that of the designed structures (see Table 5). Beyond the accuracy of the printed pore size and porosity of the samples, repeatability was found in all TPMS geometries with a volume fraction of 40%, which was calculated with the standard deviation (SD). In the case of $TPMS_S/TPMS_V$, the SD was below 0.009%, while for TPMS.Sp the highest standard deviation was 0.044 mm.

Regarding the mechanical characterisation, the experimental tests indicate that the apparent Young's modulus $E_{app,exp}$ directly depends on the volume fraction, since a higher relative density leads to a larger modulus (see Fig. 11). Consequently, TPMS structures with a volume fraction of 40% have the largest apparent moduli, specifically 403.86 MPa, 432.89 MPa and 467.33 MPa for Gyroid, Flexwave, and Cosgrid, respectively, as shown in Table A.3. In addition, we also observe that even with the same volume fraction, each TPMS structure has a different $E_{app,exp}$, which shows that, depending on the architecture of the scaffold, we can obtain a more or less rigid TPMS structure.

On the other hand, the evaluation of the numerical simulations allows estimating the apparent numerical modulus $E_{app,num}$ of each TPMS scaffold in each main direction, verifying again the isotropic behaviour of TPMS structures. Once the apparent moduli were determined, we calibrated those simulations with the purpose of mechanically characterising the lattice structures with the elastic modulus of the

Table 3
Morphometric characterisation of Flexwave TPMS structures depending on their unit cell size.

Morphometric characteristic	One RVE	Two RVEs	Three RVEs	Four RVEs	Five RVEs
RVE size [mm]	3	1.5	1	0.75	0.6
$TPMS_S/TPMS_V$ [mm^{-1}]	12.064	22.478	32.633	43.360	53.339
TPMS.Th [mm]	0.291	0.146	0.098	0.073	0.059
TPMS.Sp [mm]	0.835	0.416	0.277	0.208	0.167
TPMS.N [mm^{-1}]	1.050	2.104	3.163	4.195	5.223
DA [–]	0.099	0.118	0.117	0.124	0.008
D [–]	2.348	2.459	2.470	2.513	2.507
Conn.D [mm^{-3}]	$1.369 \cdot 10^{-11}$	$1.680 \cdot 10^{-12}$	$4.977 \cdot 10^{-13}$	$2.101 \cdot 10^{-13}$	$1.077 \cdot 10^{-13}$

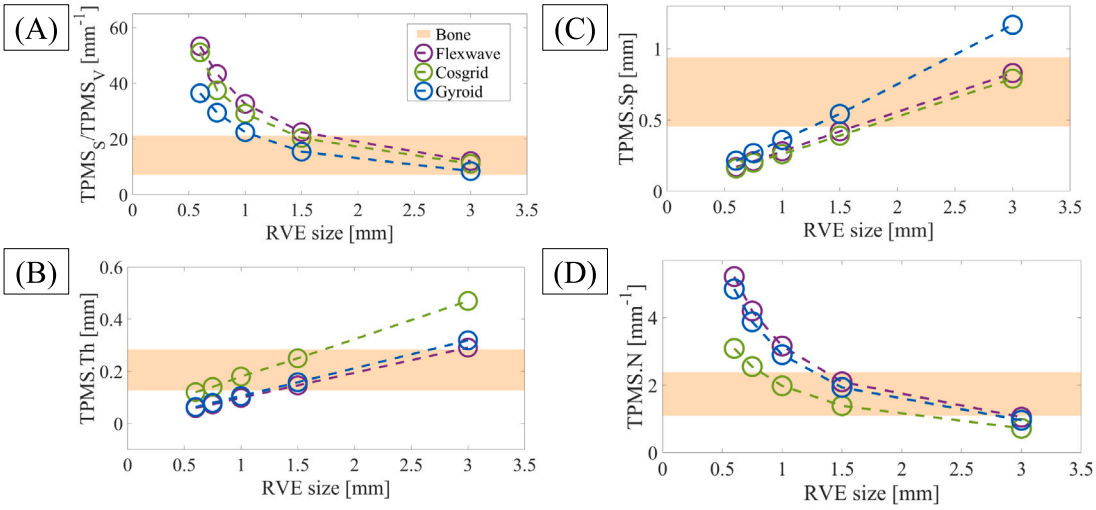

Fig. 10. Relations between TPMS RVE size and TPMS surface area (A), strut thickness (B), porosity (C) and the number of struts (D). The results from this study are displayed in purple, green and blue for each TPMS geometry, while in orange the ranges of cancellous bone are shown.

Table 4
Morphometric characterisation of TPMS structures depending on their volume fraction.

TPMS structure	$TPMS_S/TPMS_V$ [mm^{-1}]	TPMS.Th [mm]	TPMS.Sp [mm]	TPMS.N [mm^{-1}]	DA [–]	D [–]	Conn.D [mm^{-3}]
Gyroid 20%	23.462	0.102	0.602	1.939	0.007	2.365	$4.366 \cdot 10^{-13}$
Gyroid 31%	15.442	0.158	0.543	1.934	0.008	2.364	$4.366 \cdot 10^{-13}$
Gyroid 40%	11.896	0.210	0.496	1.904	0.009	2.356	$4.366 \cdot 10^{-13}$
Flexwave 20%	35.584	0.0995	0.463	1.912	0.131	2.443	$1.133 \cdot 10^{-12}$
Flexwave 31%	22.579	0.148	0.420	2.069	0.112	2.459	$1.680 \cdot 10^{-12}$
Flexwave 40%	17.093	0.193	0.396	2.081	0.104	2.454	$1.680 \cdot 10^{-12}$
Cosgrid 20%	29.392	0.254	0.420	0.947	0.009	2.454	$1.352 \cdot 10^{-12}$
Cosgrid 31%	20.456	0.260	0.397	1.324	0.009	2.464	$1.352 \cdot 10^{-12}$
Cosgrid 40%	15.967	0.285	0.3376	1.523	0.013	2.457	$1.352 \cdot 10^{-12}$

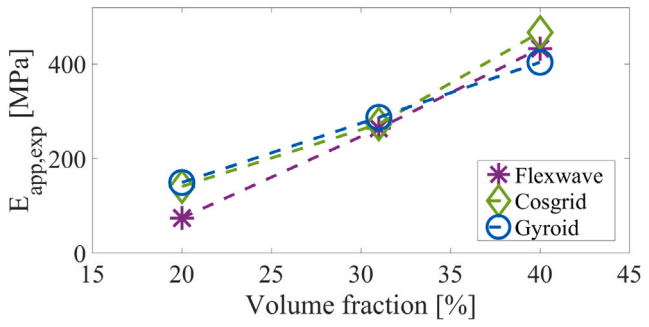

Fig. 11. Relation between apparent Young's modulus and volume fraction of all TPMS structures.

manufacturing PLA. Hence, by estimating the mean relation between the experimental and numerical apparent moduli, the measure of the Young's modulus of our printing material (PLA) can be obtained, which is 2.48 ± 0.28 GPa.

3.4. Analysis of the stress distribution in patient-specific bone-scaffold assemblies

Both healthy and osteoporotic trabecular bone cutouts show a preferred orientation of their trabeculae in the X direction, thus being stiffer along that axis. As shown in the results collected in Table 6, the largest $E_{app,num}$ under compression for the healthy cancellous bone fragment is 2062.54 MPa, whereas for the osteoporotic case it is 582.68 MPa. Bearing this in mind, we decided to evaluate three different design strategies for the bone-scaffold assemblies: first, assemblies with close microstructural characteristics to cancellous bone tissue; second, constructs with TPMS scaffolds with an apparent compression modulus

Table 5
Printability of TPMS scaffolds.

TPMS structure	$TPMS_V/TV$ [%]	Error $TPMS_V/TV$ [%]	TPMS.Sp [mm]	Error TPMS.Sp [%]
Computational Gyroid 31%	30.79	–	5.44	–
Gyroid 31%	30.43	1.17	5.33	2.04
Computational Gyroid 40%	40.10	–	4.94	–
[a]$Gyroid_1$ 40%	41.43	3.22	4.662	6.04
[a]$Gyroid_2$ 40%	40.10	0.01	4.708	4.77
Computational Flexwave 31%	30.65	–	4.15	–
Flexwave 31%	30.59	0.22	3.866	7.42
Computational Flexwave 40%	40.06	–	3.91	–
[b]Flexwave 40_1 %	39.23	2.12	3.80	2.95
[b]Flexwave 40_2 %	38.51	4.01	3.76	4.12
Computational Cosgrid 31%	34.42	–	3.941	–
Cosgrid 31%	31.90	7.89	3.68	7.16
Computational Cosgrid 40%	40.09	–	3.834	–
[c]Cosgrid 40_1 %	38.66	3.70	3.560	7.68
[c]Cosgrid 40_2 %	39.46	1.62	3.624	5.79

[a] $SD_{TPMS_V/TV}$ = 0.005%, $SD_{TPMS.Sp}$ = 0.030 mm.
[b] $SD_{TPMS_V/TV}$ = 0.005%, $SD_{TPMS.Sp}$ = 0.044 mm.
[c] $SD_{TPMS_V/TV}$ = 0.009%, $SD_{TPMS.Sp}$ = 0.032 mm.

Table 6
Apparent elastic moduli under compression for the isolated cancellous bone sections.

Trabecular bone cutout	$E_{appX,num}$ [MPa]	$E_{appY,num}$ [MPa]	$E_{appZ,num}$ [MPa]	Mean $E_{app,num}$ [MPa]
Healthy	2062.54	1047.67	1409.68	1506.63
Osteoporotic	582.68	544.95	381.60	503.07

similar to cancellous bone; and lastly, constructs composed of TPMS structures with both a morphometry and apparent elastic modulus similar to cancellous bone.

3.4.1. First strategy design: similar morphometry

In order to design bone-scaffold assemblies with a morphometry similar to trabecular bone, we first considered the Young's modulus of our printing material (E_{PLA} = 2.48 GPa) for the TPMS structures, which was 6.5 times lower than the elastic modulus of the bone tissue of the healthy sample. The results indicate that a microstructure similar to trabecular bone ensures a uniform stress transfer between bone and scaffold, since there is a notable reduction in the stress concentration in the assembly. This is shown in Fig. 12(B) and (C), where patient-specific assemblies are indicated with orange-coloured rectangles. In contrast, a different morphometry hampers this transmission, concentrating most of the stresses in the surrogate with a lower volume fraction (see Fig. 12(A) and (D)). Therefore, a patient-specific morphometry proved to be essential to observe a uniform load transfer between bone and scaffold.

Secondly, apart from PLA, we also designed patient-specific TPMS structures by selecting a conventional material for medical implants: a metal alloy. Taking into account that the Young's modulus of Ti6Al4V is about 110 GPa [34], we chose the patient-specific volume fraction of 31% and 20% for the healthy and osteoporotic metal assemblies, respectively. The results show that a morphometry similar to cancellous bone allows a homogeneous load transmission between bone and TPMS scaffold (see Fig. 13). Nevertheless, by mechanically characterising the healthy TPMS surrogate, we observe in Table A.4 that the TPMS structure with a relative density of 31% has a much larger apparent modulus (10.80 GPa) than the healthy bone sample (2062.54 MPa), which can lead to stress shielding and, lastly, to the loosening of the implant. The same occurs with the TPMS structure of 20%, whose $E_{app,num}$ is 3.36 GPa, a much higher value compared to the pathological tissue (582.68 MPa). Therefore, we concluded that, in order to avoid stress shielding phenomena with stiffer materials than bone, the scaffold's patient-specific microstructure needs to be compromised by means of greatly reducing its volume fraction. That is, by losing its morphometric patient-specificity.

3.4.2. Second strategy design: similar apparent compression elastic modulus

In this case, we first designed a TPMS structure whose numerical apparent modulus was close to the largest one of the healthy and osteoporotic cancellous bone. In other words, the TPMS scaffolds presented a mechanical patient-specificity to both types of bone. To do this, we lowered the volume fraction of the Flexwave scaffold to 12% and 6.2% for the healthy and osteoporotic case, respectively. The resulting $E_{app,num}$ is 2072.53 MPa for the healthy scaffold and 561.57 MPa for the pathological surrogate, which are close to the ones of healthy (2062.54 MPa) and pathological trabecular bone (582.68 MPa). However, these results indicate that considering mechanical patient-specific TPMS surrogates leads to a poor load bearing between both structures, concentrating most of the stresses in the highly porous TPMS scaffolds, as shown in Fig. 14.

3.4.3. Third strategy design: similar morphometry and apparent compression elastic modulus

For the third type of bone-scaffold assemblies, we decided to use a reinforcement material for PLA in order to find a combination of a base material and TPMS scaffold that most closely resembled the apparent Young's modulus of the analysed healthy bone sample. A study carried out by Efendy and Pickering (2019) [35] used harakeke and hemp fibres as reinforcement materials to enhance the mechanical properties of PLA [35]. Consequently, in order to find a stiffer material that provides optimal mechanical properties, we chose PLA reinforced with a 40 wt% of hemp fibre, whose elastic modulus (9.67 GPa) is close to that of the analysed healthy trabecular bone (11.82 GPa). By calibrating the TPMS structures with this new material (PLA40Hemp), we increased by a 23.22% the apparent elastic moduli of the TPMS scaffolds (for detailed values, see Table A.5).

Regarding the map of principal stresses in the compression direction of the healthy constructs, we see that all healthy assemblies formed of the TPMS scaffolds with the patient-specific volume fractions of 31% and 40% allow a homogeneous transmission of mechanical stresses from bone to scaffold because of the similar morphometries between both structures (see Fig. 15). However, the osteoporotic constructs composed of those same TPMS structures show little stress transfer, mainly concentrating the stresses in the osteoporotic cancellous tissue (see Fig. 16).

In the case of the healthy assemblies comprised of the TPMS structures with a relative density of 20%, the stresses mainly concentrate in the TPMS structure. Nevertheless, the similar morphometry between the TPMS scaffold and the pathological bone cutout in the osteoporotic assemblies allows a better load bearing than in the case of the healthy construct, as shown in Fig. 17. With this comparison, we verify again that a morphometry different from cancellous bone is counterproductive because of the slight stress transfer between scaffold and bone.

3.4.4. Quantitative analysis of the stress transmission in bone-scaffold assemblies

The stress in the compression direction of each bone-scaffold assembly was plotted and further analysed to quantitatively check the uniform stress distribution between bone and scaffold due to patient-specificity. The histograms show that a similar morphometry to trabecular bone is a key factor to obtaining a similar stress distribution in both structures, as shown in Fig. 18(B) and (C), where high similarities are observed in the patient-specific designs proposed in this work.

This similar stress distribution was further evaluated by estimating the Jaccard coefficient of each bone-scaffold assembly. In Table 7, it can be observed that all assemblies comprised of patient-specific TPMS structures have significantly larger Jaccard indexes than the constructs

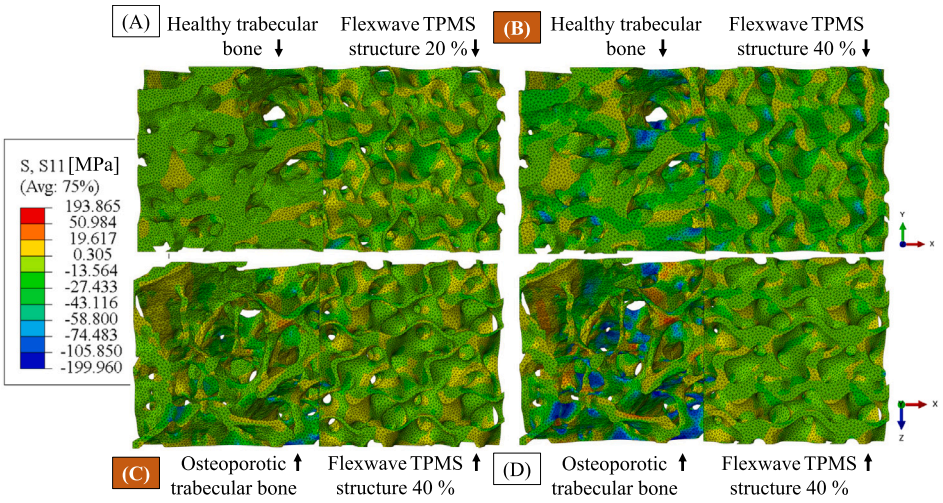

Fig. 12. Stress distribution in the compression direction when using PLA as the scaffold's material. (A) Healthy assembly containing Flexwave with a volume fraction of 20%. (B) Healthy assembly containing Flexwave with a volume fraction of 40%. (C) Osteoporotic assembly containing Flexwave with a volume fraction of 20%. (D) Osteoporotic assembly containing Flexwave with a volume fraction of 40%. Morphometric patient-specificity is indicated with orange-coloured rectangles.

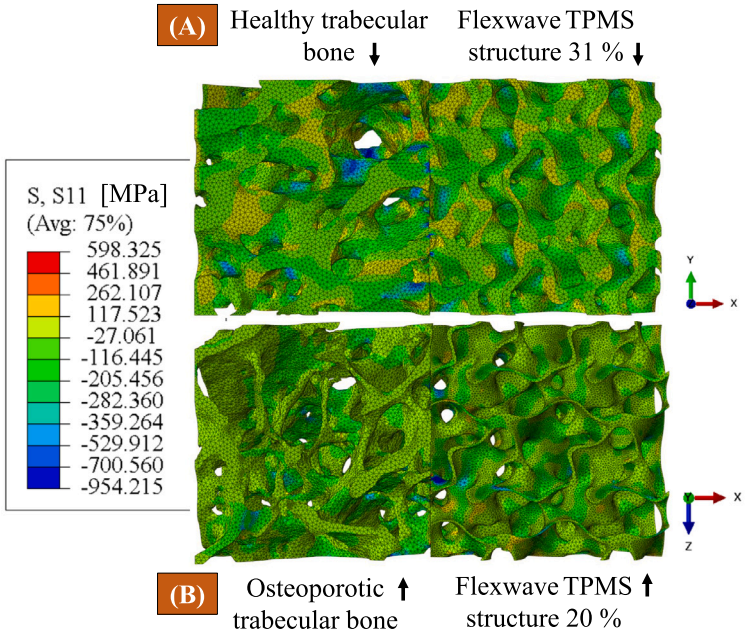

Fig. 13. Stress distribution in the compression direction when using Ti6Al4V as the scaffold's material. (A) Healthy assembly containing Flexwave with a volume fraction of 31%. (B) Osteoporotic assembly containing Flexwave with a volume fraction of 20%. Morphometric patient-specificity is indicated with orange-coloured rectangles.

with different morphometries, indicating that a similar load distribution and thereby a better stress transmission between bone and scaffold are achieved. A Jaccard index of 1 would imply a perfectly matching mechanical behaviour between bone and scaffold. Table 7 shows that matching morphometry is crucial to create a uniform mechanical environment in the construct. As a matter of fact, a consistent increase of approximately 0.2 in the Jaccard index (20%), even higher for many of the constructs evaluated, is observed by defining a patient-specific morphometry.

3.4.5. Apparent compression modulus of bone-scaffold assemblies

Once the load bearing of the bone-scaffold assemblies was evaluated under different microstructural and mechanical conditions, we analysed the resulting apparent moduli of the constructs (for detailed values, see Table A.4), which are represented in Fig. 19. All patient-specific solutions are indicated with coloured rectangles in the same figure.

PLA is a less rigid material than trabecular bone. Thus, for the first design strategy, the numerical compressions of bone-scaffold assemblies have lower apparent moduli compared to cancellous bone, which can hamper a stable mechanical environment. Specifically, the healthy patient-specific assembly has an $E_{app,num}$ of 606.20 MPa and the osteoporotic case 109.45 MPa, much lower values than the mean apparent moduli of healthy and osteoporotic tissue (1506.63 MPa and 503.07 MPa, respectively). On the other hand, when considering the Ti6Al4V metal alloy for patient-specific assemblies, the opposite occurs: the volume fractions of 31% for the healthy case and 20% for the pathological construct result in stiffer assemblies than bone (3066.30

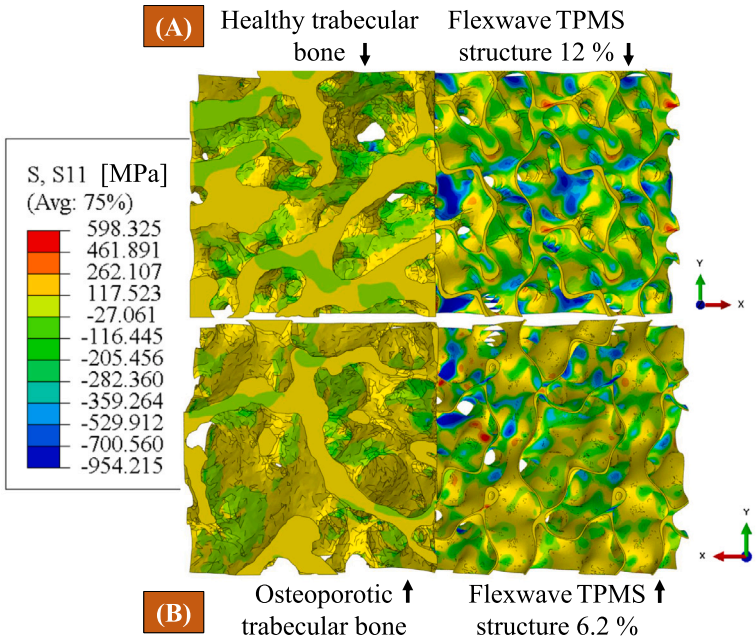

Fig. 14. Stress distribution in the compression direction when using Ti6Al4V as the scaffold's material. Due to the high porosity of the scaffolds, the fine mesh was deleted in order to better appreciate the stress concentration. (A) Healthy assembly containing Flexwave with a volume fraction of 12%. (B) Osteoporotic assembly containing Flexwave with a volume fraction of 6.2%. Mechanical patient-specificity is indicated with an orange-coloured rectangle.

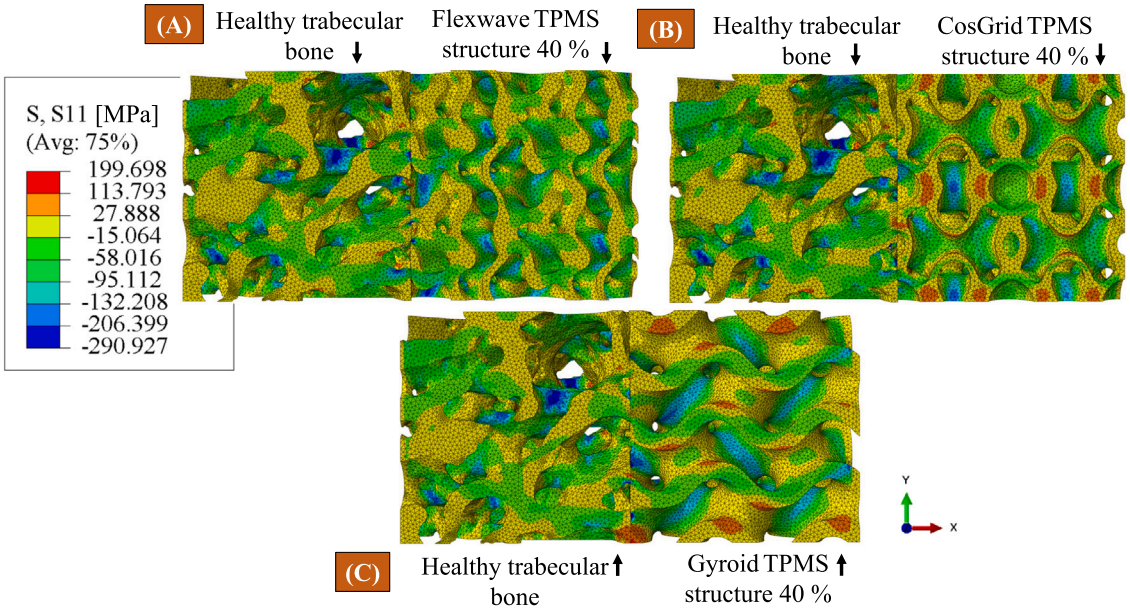

Fig. 15. Stress distribution in the compression direction when using PLA40Hemp as the scaffold's material. Healthy assemblies comprised of Flexwave (A), Cosgrid (B), and gyroid (C) TPMS structures with a relative density of 40%. Morphometric patient-specificity is indicated with orange-coloured rectangles.

MPa and 761.42 MPa, respectively), which can end up causing stress shielding.

In the case of the second design strategy, reducing the volume fraction of the metallic Flexwave TPMS scaffold to 12% leads to an apparent modulus (1482.66 MPa) similar to healthy trabecular bone, as shown in the blue box in Fig. 19. Nonetheless, as indicated before, a microstructure different from cancellous tissue can hinder a uniform load bearing in bone-scaffold constructs. Regarding the osteoporotic assemblies, the use of Flexwave with a volume fraction of 6.2% results in a construct with an $E_{app,num}$ of 372.36 MPa, which is lower than the osteoporotic trabecular bone (503.07 MPa). This difference in apparent modulus could be attributed to the slim struts of highly-porous TPMS structures, limiting the contact between the surrogates, thereby hampering stress transmission and reducing the apparent compression modulus of the bone-scaffold assembly.

Lastly, when mimicking both the morphometry and the apparent Young's modulus of trabecular bone, we observe that the healthy assembly containing the patient-specific Flexwave TPMS scaffold with a

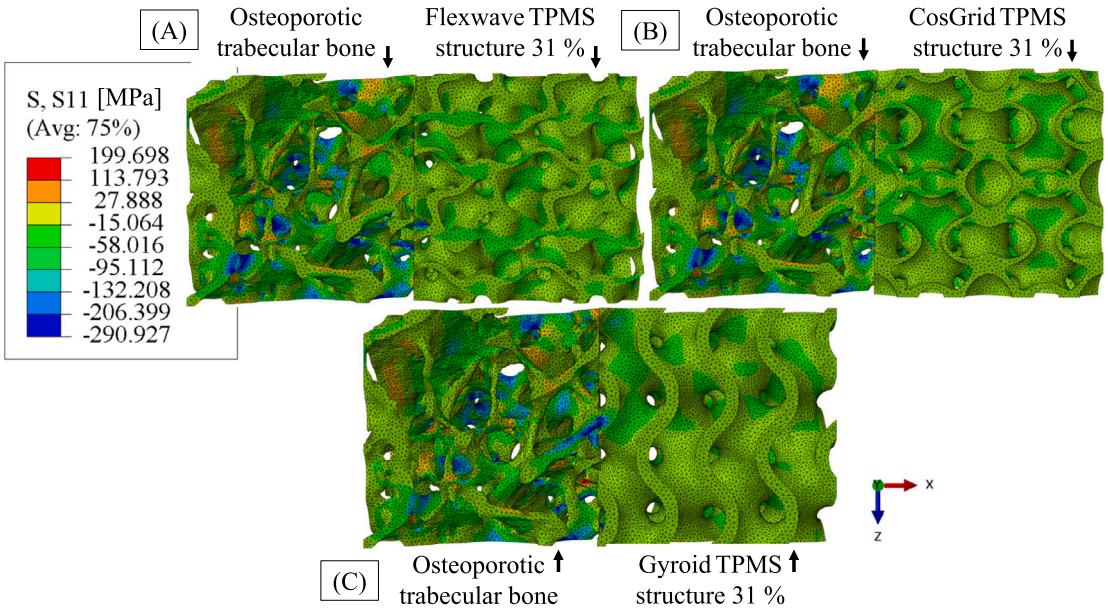

Fig. 16. Stress distribution in the compression direction when using PLA40Hemp as the scaffold's material. Osteoporotic assemblies comprised of Flexwave (A), Cosgrid (B), and gyroid (C) TPMS structures with a relative density of 31%.

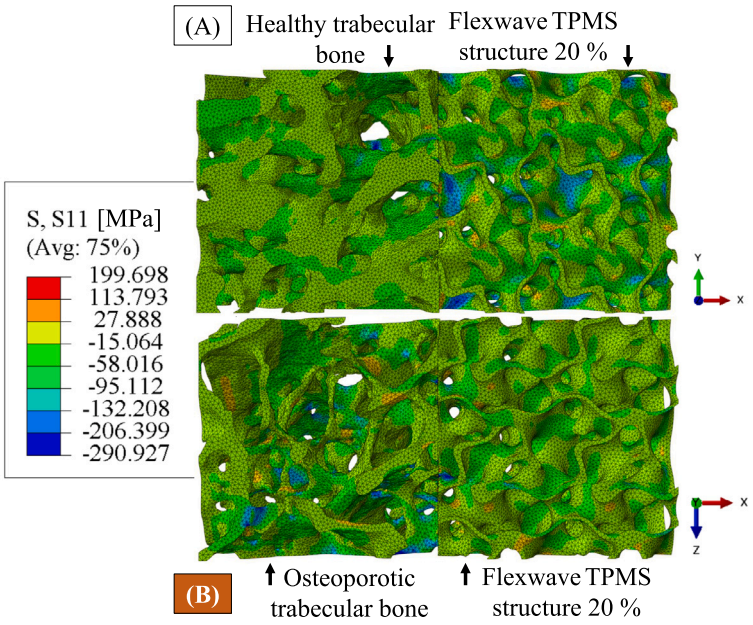

Fig. 17. Stress distribution in the compression direction when using PLA40Hemp as the scaffold's material. (A) Healthy construct containing Flexwave with a volume fraction of 20%. (B) Osteoporotic construct containing Flexwave with a relative density of 20%. Morphometric patient-specificity is indicated with orange-coloured rectangles.

relative density of 40% has an $E_{app,num}$ very close to healthy trabecular bone, 1559.06 MPa. However, the osteoporotic assembly comprised of Flexwave with the patient-specific volume fraction of 20% has a lower $E_{app,num}$ than the pathological bone (297.30 MPa versus 503.07 MPa). Therefore, following the third design strategy, we lastly explored how the geometry of the TPMS structures affected the global apparent modulus of patient-specific bone-scaffold assemblies.

The healthy assemblies composed of gyroid and Cosgrid structures with a volume fraction of 40% show an apparent modulus close to healthy trabecular bone, as depicted in Fig. 20. Specifically, the percentage changes between healthy cancellous bone and these patient-specific healthy assemblies are 3.36%, 8.44%, and 0.94% for the constructs containing Flexwave, Cosgrid and Gyroid TPMS structures, respectively. This indicates that these bone-TPMS assemblies can withstand the mechanical loads healthy trabecular bone is subjected to, thus providing a stable mechanical environment that can help osseointegrate the TPMS scaffold in the bone defect area. On the other hand, among the osteoporotic assemblies, the one comprised of Cosgrid with a volume fraction of 20% has the most similar $E_{app,num}$ to pathological bone (475.03 MPa and 503.07 MPa, respectively). The percentage changes

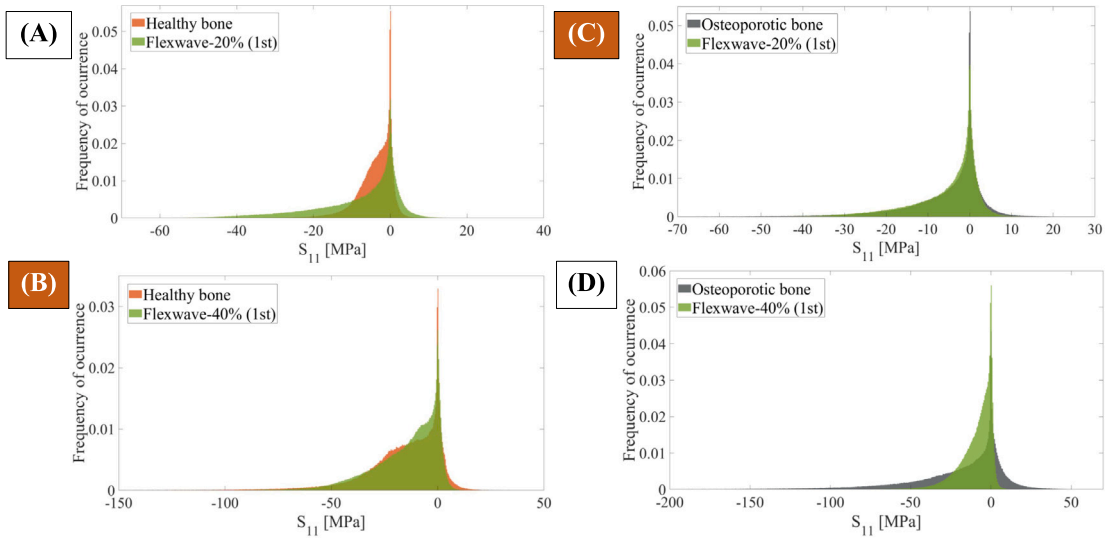

Fig. 18. Histograms of the stress distribution in the compression direction when following the first design strategy. (A) Healthy construct containing Flexwave with a volume fraction of 20%. (B) Healthy construct containing Flexwave with a volume fraction of 40%. (C) Osteoporotic construct containing Flexwave with a volume fraction of 20%. (D) Osteoporotic construct containing Flexwave with a volume fraction of 40%. Microstructural patient-specificity is indicated with an orange-coloured rectangle.

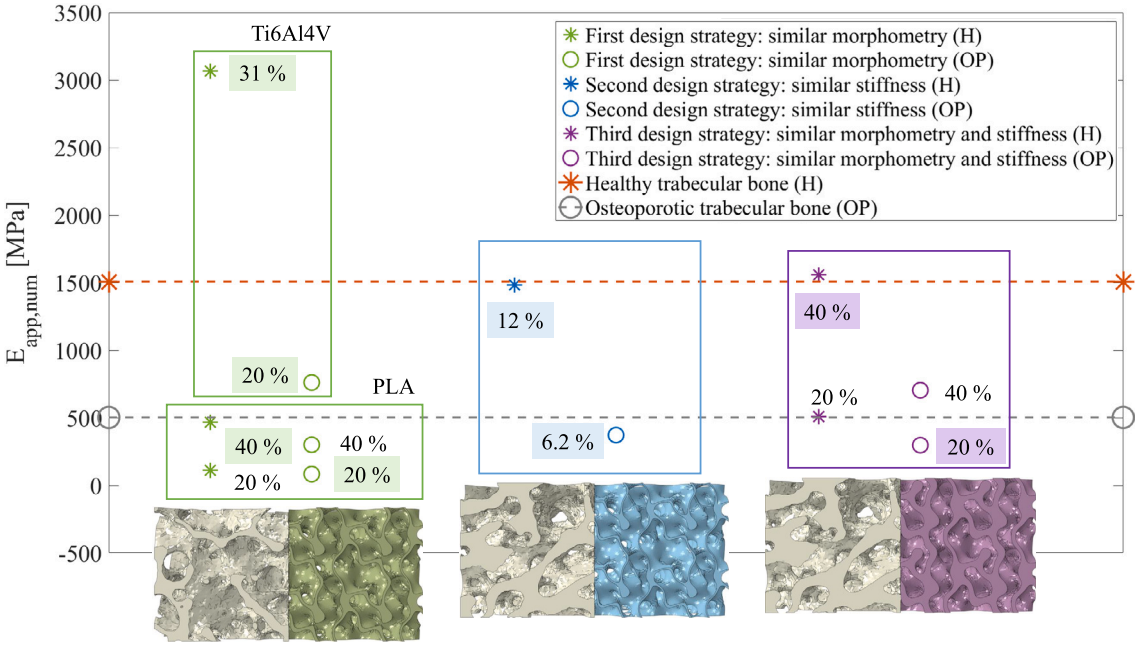

Fig. 19. Representation of the apparent elastic moduli of each healthy and osteoporotic assembly containing the Flexwave scaffold with different volume fractions depending on the design strategy. All healthy cases are indicated with star markers, whereas the pathological ones are depicted with circle markers. The mean apparent modulus of osteoporotic and healthy bone is represented with a discontinued grey and orange line, respectively. Next to each assembly the volume fraction of the TPMS surrogate is specified indicating, when coloured, a patient-specific solution.

in this case are 40.9%, 5.57%, and 21.40% for the patient-specific constructs containing Flexwave, Cosgrid and Gyroid TPMS structures, respectively. Hence, it can be observed that, for the same volume fraction, the mechanical response of bone-scaffold assemblies depends on the geometry of the TPMS structure they are composed of.

4. Discussion

Bone conduction, which is the process by which bone ingrowth takes place, is ruled by the microstructure of the scaffold [36]. This way, in order to design surrogates that mimic bone morphometry, unit cell size, porosity, pore size and surface area need to be controlled [37]. On the one hand, we assessed the optimal dimension of RVEs in patient-specific gyroid TPMS structures. We discovered that for a volume fraction of 31%, an RVE size ranging from 1.5 mm to 3 mm matches trabecular bone surface area, trabecular thickness, pore size and number of trabeculae. Kumar et al. (2024) [37] also studied the optimal unit cell size for a required porosity percentage and surface area volume ratio (SA/V) in different TPMS architectures and concluded that the most favourable RVE dimension was between 2 mm to 5 mm for a porosity ranging from 70% to 80%. Thus, according to these authors, a unit cell size of 2 mm is optimal for a relative density of 30%, which is within range of our own results for patient-specific TPMS structures with a volume fraction of 31%.

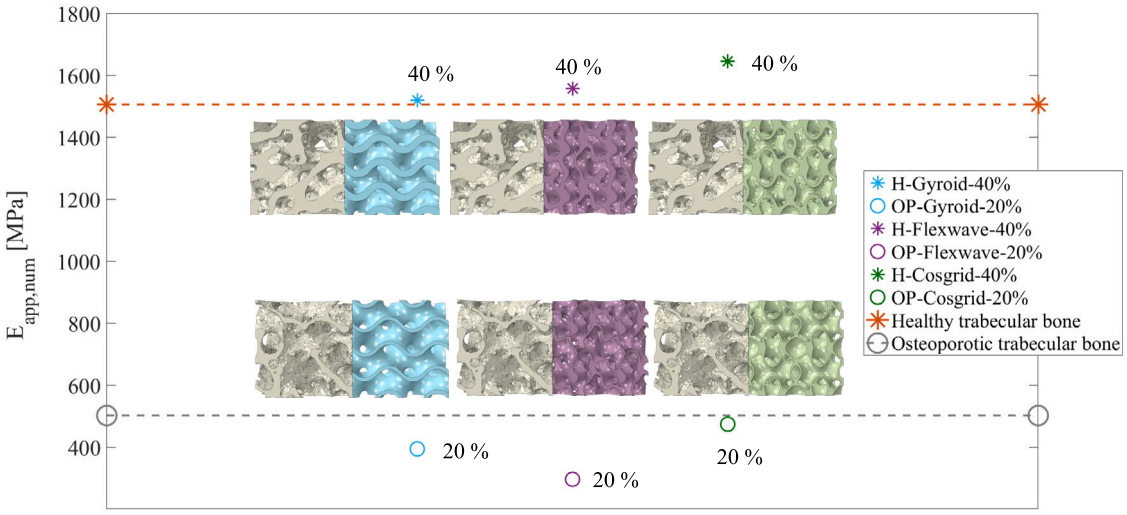

Fig. 20. Representation of the apparent numerical moduli of patient-specific bone-scaffold assemblies composed of each TPMS surrogate studied in this work. All healthy cases are indicated with star markers, whereas the pathological ones are depicted with circle markers. The mean apparent modulus of osteoporotic and healthy trabecular bone are represented with discontinued grey and orange lines, respectively.

Table 7
Jaccard index of bone-scaffold constructs for each design strategy.

Bone-scaffold assembly	Design strategy	Jaccard index
H-Flexwave-20% (PLA)	1st	0.575
[a]H-Flexwave-40% (PLA)		[a]0.845
[a]OP-Flexwave-20% (PLA)		[a]0.872
OP-Flexwave-40% (PLA)		0.515
[a]H-Flexwave-31% (Ti)		[a]0.806
[a]OP-Flexwave-20% (Ti)		[a]0.895
H-Flexwave-12%	2nd	0.379
OP-Flexwave-6.2%		0.515
H-Gyroid-20%	3rd	0.594
[a]H-Gyroid-31%		[a]0.810
[a]H-Gyroid-40%		[a]0.887
H-Flexwave-20%		0.555
[a]H-Flexwave-31%		[a]0.806
[a]H-Flexwave-40%		[a]0.852
H-Cosgrid-20%		0.632
[a]H-Cosgrid-31%		[a]0.829
[a]H-Cosgrid-40%		[a]0.838
[a]OP-Gyroid-20%		[a]0.780
OP-Gyroid-31%		0.653
OP-Gyroid-40%		0.576
[a]OP-Flexwave-20%		[a]0.893
OP-Flexwave-31%		0.653
OP-Flexwave-40%		0.542
[a]OP-Cosgrid-20%		[a]0.752
OP-Cosgrid-31%		0.594
OP-Cosgrid-40%		0.508

[a] Morphometric patient-specificity is indicated. First, second and third design strategies tackle morphometric, mechanical and both mechanical and morphometric patient-specificity, respectively.

On the other hand, previous studies have stated that in order to minimise pore obstruction and provide a favourable surface area for cell adhesion, which in turn allows imitating fluid transport properties of bone, the pore size of bone scaffolds should be between 100 μm to 700 μm and the porosity should be higher than 50% [38]. The results of the present study demonstrate that the design of patient-specific TPMS scaffolds with relative densities of 31% and 40% allows obtaining favourable pore sizes for bone ingrowth, as shown in Table 4.

Two of the most common conditions under which femur prostheses fail are aseptic loosening, which is mainly caused by bone loss due to a higher stiffness in the orthopaedic implant than in bone, and implant fracture [39–41]. In fact, when metal implants are much stiffer than the host bone, additional and extensive revision surgery is needed. According to Labek et al. (2011) [42], total hip replacements undergo revision surgery in the 6.45% of cases after five years and in the 12.9% of cases after ten years, while after 25 years half of the patients are expected to undergo revision surgery. In that regard, in the present work, we have deemed it decisive to observe the interaction and mechanical stability between bone and TPMS structures under different design and mechanical conditions. Our results state that a uniform stress transmission from bone to scaffold depends on morphometry, resulting in a homogeneous load transfer when considering a scaffold microstructure similar to that of trabecular bone. However, the scaffold material is a key factor. This has been observed using the conventional Ti6Al4V metallic alloy. Patient-specific scaffold solutions composed of this metal reach much higher stiffnesses than bone (first design strategy), which can lead to bone loss and eventually result in implant loosening. Nevertheless, the analysis of the second strategy design, which considers patient-specificity by matching apparent mechanical properties, reveals a poor mechanical environment for bone formation compared to morphometry-based strategies. Thus, both a morphometry and an apparent elastic modulus similar to cancellous bone play a significant role in avoiding stress shielding and providing a stable mechanical environment. Other results in the literature support our findings. Masud Rana et al. (2021) [43] proposed a novel method to design biomimetic bone scaffolds based on Computer Tomography (CT) scan data by cutting out three sections of human femur bone and replacing them with porous and solid implants. Their results revealed that patient-specific porous scaffolds had stress and strain profiles similar to those of adjacent bone compared to solid scaffolds, which could lead to better bone growth. Markus Laubach et al. (2022) [44] designed patient-specific, biodegradable, and medical grade bone scaffolds for four clinical cases with complex post-traumatic lower long bone defects. Cases 1, 3 and 4 showed bony ingrowth and a fully interconnected scaffold with osseous bridges at the bony ends. Full weight bearing was accomplished in patient 2 23 months after scaffold implantation. Lastly, Elenskaya et al. (2025) [19] proposed a TPMS design approach based on the micro-CT model of a reference bone to tailor the morphometry

and mechanical behaviour of the scaffold. They successfully achieved the design of several patient-specific TPMS scaffolds with a mechanical response similar to the reference model by controlling the spatial orientation of the unit cell.

However, this study has some limitations. First, the anisotropy found in trabecular bone was not replicated in the design of TPMS scaffolds during this study. Zhichao Luo et al. (2024) [45] studied the effect of the aspect ratio on the anisotropy of elastic mechanical properties and on the deformation behaviour of four types of TPMS structures. They found, through experimental characterisation, that with an aspect ratio of 2 in the [001] direction, the elastic modulus, maximum stress, and energy absorption of the TPMS structures greatly improved. Josette Vigil et al. (2024) [46] designed TPMS scaffolds that consisted of three phase regions with volume fractions of 25%, 25% and 50% and with materials with soft, medium, and hard stiffness properties, respectively. By means of multiphase TPMS scaffolds, they confirmed that varying the layering patterns in the longitudinal and transverse directions resulted in tunable anisotropic material properties. Secondly, our study highly depends on the micro-CT imaging technique in order to obtain the microstructural characteristics of cancellous bone and design patient-specific TPMS scaffolds accordingly. The main issue with this technology is that due to its high-radiation sources and high-security zones it cannot be applied in clinical practice [47]. Therefore, the use of micro-CT is limited to *ex vivo* analyses, thus not allowing the *in vivo* characterisation of bone in a patient [48]. Consequently, High-Resolution Peripheral Quantitative Computer Tomography (HR-pQCT) is deemed to be the best scan to measure bone morphometry *in vivo* [48]. However, this imaging technique is limited to extremities, such as the distal radius and tibia, with a long scanning time and a reduced resolution [48,49]. Hence, it is crucial to study new imaging technologies of low radiation and high resolution that enable the characterisation of trabecular microstructure located at any part of the human body. Thirdly, in this work we have studied the influence of a similar morphometry to bone on the design of bone substitutes and the distribution of mechanical stresses in ideal bone-scaffold assemblies. However, this study does not address the role of the shape of patient-specific bone defects in scaffold design, where complex bone boundaries might lead to incomplete edge unit cells and thus impact the mechanical performance and integrity of the bone scaffold.

5. Conclusions

This work aims to evaluate three design strategies of patient-specific bone-scaffold assemblies in order to create a uniform mechanical environment. To that end, we have considered the following cases: first, constructs with scaffolds matching bone microstructure; second, assemblies with surrogates with an apparent Young's modulus similar to cancellous bone; and third, constructs with bone substitutes mimicking both the morphometry and the apparent modulus of trabecular bone.

Exploring the relation between morphometry and the representative volume element size of TPMS structures reveals that an RVE size between 1.5 mm and 3 mm in the patient-specific configurations (BV/TV of 31%) matches the requirements of surface area, mean trabecular thickness, pore size, and number of trabeculae. In the case of Cosgrid TPMS scaffolds, the strut thickness and number of struts mimic bone morphometry when considering a smaller unit cell size than in the case of Flexwave and Gyroid structures, which would involve a finer and more complicated manufacturing.

Regarding the mechanical characterisation of TPMS structures, by means of compression tests, our results give away a clear positive linear correlation between volume fraction and apparent modulus. Moreover, it was demonstrated that both the morphometry and the apparent elastic modulus of TPMS scaffolds can be adjusted by the volume fraction, thus mirroring the microstructural and mechanical characteristics of trabecular bone.

Lastly, by means of mechanically characterising the finite element models of bone-scaffold assemblies, we observed that patient-specific TPMS structures are capable of transmitting mechanical stresses in a homogeneous manner when matching the microarchitecture of cancellous bone. This was quantitatively evaluated by estimating the Jaccard index. Our results show that the stress distribution in patient-specific TPMS scaffolds is 83.86 ± 3.71% similar to that of the target bone, while non-patient-specific TPMS surrogates exhibit a similarity of 54.41 ± 5.98%. This demonstrates that a patient-specific TPMS scaffold design considering a morphometry and an apparent elastic modulus aligned with the trabecular bone is essential to reduce stress shielding phenomena and stimulate the osseointegration of the bone substitute in the bone defect area. Therefore, in order to design an adequate bone scaffold, it is necessary to find a compromise between its patient-specific microstructure and stiffness.

CRediT authorship contribution statement

Andrea Fresquet-Monter: Writing – review & editing, Writing – original draft, Visualization, Validation, Methodology, Investigation, Data curation, Conceptualization. **Ricardo Belda:** Writing – review & editing, Writing – original draft, Visualization, Supervision, Software, Methodology, Investigation, Conceptualization. **Ana Vercher-Martínez:** Writing – review & editing, Writing – original draft, Supervision, Project administration, Funding acquisition, Conceptualization. **Raquel Megías:** Writing – review & editing, Validation, Software, Investigation, Formal analysis. **Eugenio Giner:** Writing – review & editing, Supervision, Project administration, Funding acquisition.

Ethics statement

The authors did not perform experiments involving human participants or animals.

Declaration of competing interest

The authors declare that they have no known competing financial interests or personal relationships that could have appeared to influence the work reported in this paper.

Acknowledgements

The authors acknowledge the Ministerio de Ciencia e Innovación y Universidades and the European Regional Development Fund (FEDER) for the financial support received through the projects PID2020-118920RB-I00 and PID2023-151610OB-C22 funded by MCIN/AEI /10.13039/501100011033, the Generalitat Valenciana PROMETEO/2021/046, CIGE/2023/110 and CIACIF/2023/454, and CRUE-Universitat Politècnica de València.

Appendix. Additional tables

See Tables A.1–A.5.

Data availability

The datasets generated and/or analysed during the current study are available from the corresponding author on reasonable request.

Table A.1
Morphometric characterisation of the Cosgrid TPMS structures depending on their unit cell size.

Morphometric characteristic	One RVE	Two RVEs	Three RVEs	Four RVEs	Five RVEs
RVE size [mm]	3	1.5	1	0.75	0.6
$TPMS_S/TPMS_V$ [mm^{-1}]	11.093	20.334	29.140	37.509	51.120
TPMS.Th [mm]	0.471	0.249	0.178	0.140	0.115
TPMS.Sp [mm]	0.778	0.394	0.262	0.196	0.156
TPMS.N [mm^{-1}]	0.721	1.389	1.976	2.548	3.092
DA [–]	0.008	0.012	0.006	0.009	0.007
D [–]	2.355	2.464	2.472	2.513	2.647
Conn.D [mm^{-3}]	$1.13 \cdot 10^{-11}$	$1.352 \cdot 10^{-12}$	$3.998 \cdot 10^{-13}$	$1.689 \cdot 10^{-13}$	$8.644 \cdot 10^{-14}$

Table A.2
Morphometric characterisation of the Gyroid TPMS structures depending on their unit cell size.

Morphometric characteristic	One RVE	Two RVEs	Three RVEs	Four RVEs	Five RVEs
RVE size [mm]	3	1.5	1	0.75	0.6
$TPMS_S/TPMS_V$ [mm^{-1}]	8.449	15.442	22.455	29.448	36.439
TPMS.Th [mm]	0.319	0.158	0.105	0.079	0.063
TPMS.Sp [mm]	1.169	0.543	0.359	0.268	0.214
TPMS.N [mm^{-1}]	0.961	1.934	2.906	3.878	4.855
DA [–]	0.0107	*0.0081*	0.0086	0.0098	0.0087
D [–]	2.260	2.364	2.376	2.420	2.413
Conn.D [mm^{-3}]	$1.770 \cdot 10^{-8}$	$7.723 \cdot 10^{-9}$	$1.270 \cdot 10^{-13}$	$5.326 \cdot 10^{-14}$	$2.720 \cdot 10^{-14}$

Table A.3
Experimental apparent moduli under compression of the analysed TPMS scaffolds.

TPMS structure	$E_{app,exp}$ [MPa]
Gyroid TPMS 20%	149.50 ± 2.29
Gyroid TPMS 31%	287.49 ± 8.48
Gyroid TPMS 40%	403.86 ± 3.14
Flexwave TPMS 20%	74.43 ± 1.65
Flexwave TPMS 31%	264.05 ± 2.81
Flexwave TPMS 40%	432.89 ± 29.53
Cosgrid TPMS 20%	141.02 ± 3.65
Cosgrid TPMS 31%	273.35 ± 31.41
Cosgrid TPMS 40%	467.33 ± 17.13

Table A.4
Numerical apparent moduli of bone-scaffold constructs for each design strategy.

Bone-scaffold assembly	1st design strategy: $E_{app,num}$ [MPa]	2nd design strategy: $E_{app,num}$ [MPa]	3rd design strategy: $E_{app,num}$ [MPa]
H-Gyroid-20%	–	–	777.88
H-Gyroid-31%	–	–	1149.45
H-Gyroid-40%	–	–	1520.94
H-Flexwave-12%	–	1482.66	–
H-Flexwave-20%	152.82 (PLA)	–	511.20
H-Flexwave-31%	3066.30 (Ti6Al4V)	–	1141.77
H-Flexwave-40%	606.20 (PLA)	–	1559.06
H-Cosgrid-20%	–	–	857.34
H-Cosgrid-31%	–	–	1329.55
H-Cosgrid-40%	–	–	1645.55
OP-Gyroid-20%	–	–	395.43
OP-Gyroid-31%	–	–	547.29
OP-Gyroid-40%	–	–	652.91
OP-Flexwave-6.2%	–	372.36	–
OP-Flexwave-20%	109.45 (PLA) 761.42 (Ti6Al4V)	-	297.30
OP-Flexwave-31%	–	–	569.22
OP-Flexwave-40%	367.82 (PLA)	–	704.12
OP-Cosgrid-20%	–	–	475.03
OP-Cosgrid-31%	–	–	638.24
OP-Cosgrid-40%	–	–	747.28

Table A.5
Numerical apparent moduli under compression of TPMS scaffolds when using PLA reinforced with a 40 wt% of hemp fibre (PLA40Hemp).

TPMS structure	$E_{app,num}$ [MPa]
Gyroid TPMS 20%	742.93
Gyroid TPMS 31%	1237.84
Gyroid TPMS 40%	1738.90
Flexwave TPMS 20%	397.26
Flexwave TPMS 31%	1136.94
Flexwave TPMS 40%	1863.90
Cosgrid TPMS 20%	712.73
Cosgrid TPMS 31%	1176.96
Cosgrid TPMS 40%	2012.18

References

[1] L. Vidal, C. Kampleitner, et al., Reconstruction of large skeletal defects: Current clinical therapeutic strategies and future directions using 3D printing, Front. Bioeng. Biotechnol. 8 (2020) 61, http://dx.doi.org/10.3389/fbioe.2020.00061.

[2] S.J. Tsang, N. Ferreira, et al., The reconstruction of critical bone loss: the holy grail of orthopaedics, Bone Jt. Res. 11 (6) (2022) 409–412, http://dx.doi.org/10.1302/2046-3758.116.BJR-2022-0186.

[3] J. Zhang, X. Chen, et al., Design of a biomimetic graded TPMS scaffold with quantitatively adjustable pore size, Mater. Des. (2022) http://dx.doi.org/10.1016/j.matdes.2022.110665.

[4] E. So, V.H. Mandas, et al., Large osseous defect reconstruction using a custom three-dimensional printed titanium truss implant, J Foot Ankle Surg. 57 (1) (2018) 196–204, http://dx.doi.org/10.1053/j.jfas.2017.07.019.

[5] C. Kiernan, C. Knuth, et al., Chapter 6 - endochondral ossification: Recapitulating bone development for bone defect repair, in: Developmental Biology and Musculoskeletal Tissue Engineering, Academic Press, 2018, pp. 125–148, http://dx.doi.org/10.1016/B978-0-12-811467-4.00006-1.

[6] C. Papakostidis, P.V. Giannoudis, Reconstruction of infected long bone defects: Issues and challenges, Injury 54 (3) (2023) 807–810, http://dx.doi.org/10.1016/j.injury.2023.01.052.

[7] A. Fallah, M. Altunbek, et al., 3D printed scaffold design for bone defects with improved mechanical and biological properties, J. Mech. Behav. Biomed. Mater. 134 (2022) 105418, http://dx.doi.org/10.1016/j.jmbbm.2022.105418.

[8] W. Wang, K.W.K. Yeung, Bone grafts and biomaterials substitutes for bone defect repair: A review, Bioact. Mater. 2 (4) (2017) 224–247, http://dx.doi.org/10.1016/j.bioactmat.2017.05.007.

[9] J. Zhu, S. Zou, et al., Additively manufactured scaffolds with optimized thickness based on triply periodic minimal surface, Materials 15 (20) (2022) 7084, http://dx.doi.org/10.3390/ma15207084.

[10] D. Karaman, H. Ghahramanzadeh Asl, The effects of sheet and network solid structures of similar TPMS scaffold architectures on permeability, wall shear stress, and velocity: A CFD analysis, Med. Eng. Phys. 118 (2023) 104024, http://dx.doi.org/10.1016/j.medengphy.2023.104024.

[11] Z. Dong, X. Zhao, Application of TPMS structure in bone regeneration, Eng. Regen. 2 (2021) 154–162, http://dx.doi.org/10.1016/j.engreg.2021.09.004.

[12] R. Belda, R. Megías, et al., Numerical analysis of the influence of triply periodic minimal surface structures morphometry on the mechanical response, Comput. Methods Programs Biomed. 230 (2023) 107342, http://dx.doi.org/10.1016/j.cmpb.2023.107342.

[13] R. Verma, J. Kumar, et al., Design and analysis of biomedical scaffolds using TPMS-based porous structures inspired from additive manufacturing, Coatings 12 (6) (2022) 839.

[14] X. Peng, Y. Huo, et al., Controlled mechanical and mass-transport properties of porous scaffolds through hollow strut, Int. J. Mech. Sci. 248 (2023) 108202, http://dx.doi.org/10.1016/j.ijmecsci.2023.108202.

[15] I. Maskery, L. Sturm, et al., Insights into the mechanical properties of several triply periodic minimal surface lattice structures made by polymer additive manufacturing, Polymer 152 (2018) 62–71, http://dx.doi.org/10.1016/j.polymer.2017.11.049.

[16] E. Maevskaia, J. Guerrero, et al., Triply periodic minimal surface-based scaffolds for bone tissue engineering: A mechanical, in vitro and in vivo study, Tissue Eng. Part A (2023) http://dx.doi.org/10.1089/ten.tea.2023.0033.

[17] M. Selim, H.M. Mouse, et al., Innovative designs of 3D scaffolds for bone tissue regeneration: Understanding principles and addressing challenges, Eur. Polym. J. 215 (2024) 113251, http://dx.doi.org/10.1016/j.eurpolymj.2024.113251.

[18] A.K. Mishra, H. Chavan, et al., Effect of cell size and wall thickness on the compression performance of triply periodic minimal surface based AlSi10Mg lattice structures, Thin-Walled Struct. 193 (2023) 111214, http://dx.doi.org/10.1016/j.tws.2023.111214.

[19] N. Elenskaya, M. Tashkinnov, et al., TPMS-based scaffolds: Adaptation of morphological properties and mechanical response to reference tissue, Int. J. Solids Struct. 315 (2025) 113366, http://dx.doi.org/10.1016/j.ijsolstr.2025.113366.

[20] S. Toosi, M.J. Javid-Naderi, et al., Additively manufactured porous scaffolds by design for treatment of bone defects, Front. Bioeng. Biotechnol. 11 (2024) 1252636, http://dx.doi.org/10.3389/fbioe.2023.1252636.

[21] R. Megías Díaz, Analysis of Osteoporosis Effect on the Mechanical Behaviour and Morphometry of Human Cancellous Bone (Ph.D. thesis), UPV, Valencia (Spain), 2024, http://dx.doi.org/10.4995/Thesis/10251/206355.

[22] M. Jaber, P.S.P. Poh, et al., PCL strut-like scaffolds appear superior to gyroid in terms of bone regeneration within a long bone large defect: An in silico study, Front. Bioeng. Biotechnol. 10 (2022) 995266, http://dx.doi.org/10.3389/fbioe.2022.995266.

[23] Y. Li, J. Li, et al., The design of strut/TPMS-based pore geometries in bioceramic scaffolds guiding osteogenesis and angiogenesis in bone regeneration, Mater. Today Bio 20 (2023) 100667, http://dx.doi.org/10.1016/j.mtbio.2023.100667.

[24] S. Ma, Q. Tang, et al., Manufacturability, mechanical properties, mass-transport properties and biocompatibility of triply periodic minimal surface (TPMS) porous scaffolds fabricated by selective laser melting, Mater. Des. 195 (2020) 09034, http://dx.doi.org/10.1016/j.matdes.2020.109034.

[25] W.L. Roque, K. Arcaro, et al., Mechanical competence of bone: A new parameter to grade trabecular bone fragility from tortuosity and elasticity, IEEE Trans. Biomed. Eng. 60 (2013) 1363–1370, http://dx.doi.org/10.1109/TBME.2012.2234457.

[26] W.L. Roque, A. Alberich-Bayarri, Tortuosity influence on the trabecular bone elasticity and mechanical competence, Dev. Med. Image Process. Comput. Vis. 19 (2015) 173–191, http://dx.doi.org/10.1007/978-3-319-13407-9.

[27] T. Hildebrand, A. Laib, et al., Direct three-dimensional morphometric analysis of human cancellous bone: Microstructural data from spine, femur, iliac crest, and calcaneus, J. Bone Miner. Res. 14 (7) (2009) 1167–1174, http://dx.doi.org/10.1359/jbmr.1999.14.7.1167.

[28] O. Al-Ketan, R.K. Abu Al-Rub, MSLattice: A free software for generating uniform and graded lattices based on triply periodic minimal surfaces, Mater. Des. Process. Commun. 3 (6) (2020) e205, http://dx.doi.org/10.1002/mdp2.205.

[29] H. Tanoto, H. Fan, et al., Quantifying the relation between aging-related trabecular bone microstructure and mechanical properties with digital volume correlation approach, Extrem. Mech. Lett. 73 (2024) 102265, http://dx.doi.org/10.1016/j.eml.2024.102265.

[30] C. Bregoli, C. Alberto Biffi, et al., Effect of trabecular architectures on the mechanical response in osteoporotic and healthy human bone, Med. Biol. Eng. Comput. 62 (2024) 3263–3281, http://dx.doi.org/10.1007/s11517-024-03134-8.

[31] A. Sherif El-Gizawy, X. Ma, et al., Characterization of microarchitectures, stiffness and strength of human trabecular bone using micro-computed tomography (micro-CT) scans, Biomed 3 (1) (2023) 89–100, http://dx.doi.org/10.3390/biomed3010007.

[32] X. Yang, Q. Yang, et al., Effect of volume fraction and unit cell size on manufacturability and compressive behaviors of Ni-Ti triply periodic minimal surface lattices, Addit. Manuf. 54 (2022) http://dx.doi.org/10.1016/j.addma.2022.102737.

[33] How to evaluate a segmentation? Link: https://vincmazet.github.io/bip/segmentation/evaluation.html.

[34] Q. Li, Q. Li, et al., Spatial topological structure design of porous Ti-6Al-4V alloy with low modulus and magnetic susceptibility, Nanomaterials 13 (24) (2023) 3113, http://dx.doi.org/10.3390/nano13243113.

[35] M.G. Aruan Efendy, K.L. Pickering, Comparison of strength and Young modulus of aligned discontinuous fibre PLA composites obtained experimentally and from theoretical prediction models, Compos. Struct. 208 (2019) 556–573, http://dx.doi.org/10.1016/j.compstruct.2018.10.057.

[36] J. Ma, Y. Li, et al., Novel 3D printed TPMS scaffolds: microstructure, characteristics and applications in bone regeneration, J. Tissue Eng. 15 (2024) http://dx.doi.org/10.1177/20417314241263.

[37] R. Kumar, J. Ramkumar, et al., Design and parametrization of TPMS lattice using computational and experimental approach, Eng. Res. Express 6 (3) (2024) http://dx.doi.org/10.1088/2631-8695/ad7109.

[38] J. Kumar, R. Verma, et al., Mechanical property analysis of triply periodic minimal surface inspired porous scaffold for bone applications: a compromise between desired mechanical strength and additive manufacturability, J. Mater. Eng. Perform. 32 (7) (2022) 3335–3347, http://dx.doi.org/10.1007/s11665-022-07322-1.

[39] N. Reznikov, O.R. Boughton, et al., Individual response variations in scaffold-guided bone regeneration are determined by independent strain- and injury-induced mechanisms, Biomaterials 194 (2019) 183–194, http://dx.doi.org/10.1016/j.biomaterials.2018.11.026.

[40] L. Liu, C. Liu, et al., Design and performance analysis of 3D-printed stiffness gradient femoral scaffold, J. Orthop. Surg. Res. 18 (2023) 120, http://dx.doi.org/10.1186/s13018-023-03612-z.

[41] S. Safavi, Y. Yu, et al., Additively manufactured controlled porous orthopedic joint replacement designs to reduce bone stress shielding: a systematic review, J. Orthop. Surg. Res. 18 (2023) 42, http://dx.doi.org/10.1186/s13018-022-03492-9.

[42] Y. Katz, Z. Yoshibash, et al., Strain shielding for cemented hip implants, Clin. Biomech. 77 (2020) 105027, http://dx.doi.org/10.1016/j.clinbiomech.2020.105027.

[43] M. Rana, A. Chaudhuri, et al., Design of patient specific bone stiffness mimicking scaffold, J. Eng. Med. 235 (12) (2021) 1453–1462, http://dx.doi.org/10.1177/09544119211030715.

[44] M. Laubach, S. uresh, et al., Clinical translation of a patient-specific scaffold-guided bone regeneration concept in four cases with large long bone defects, J. Orthop. Transl. 34 (2022) 73–84, http://dx.doi.org/10.1016/j.jot.2022.04.004.

[45] Z. Luo, Q. Tang, et al., Effect of aspect ratio on mechanical anisotropy of lattice structures, Int. J. Mech. Sci. 276 (2024) 109369, http://dx.doi.org/10.1016/j.ijmecsci.2024.109369.

[46] J. Vigiel, K. Lewis, et al., Design, fabrication, and characterization of 3D-printed multiphase scaffolds based on triply periodic minimal surfaces, Adv. Polym. Technol. 2024 (1) (2024) http://dx.doi.org/10.1155/2024/4616496.

[47] J. Pallua, D. Putzer, et al., Characterizing the mechanical behavior of bone and bone surrogates in compression using pQCT, Materials 15 (14) (2022) 5065, http://dx.doi.org/10.3390/ma15145065.

[48] K. Mys, P. Varga, et al., Correlation between cone-beam computed tomography and high-resolution peripheral computed tomography for assessment of wrist bone microstructure, J. Bone Miner. Res. 34 (5) (2019) 867–874, http://dx.doi.org/10.1002/jbmr.3673.

[49] D.E. Whittier, S.K. Boyd, et al., Guidelines for the assessment of bone density and microarchitecture in vivo using high-resolution peripheral quantitative computed tomography, Osteoporos Int. 31 (2020) 1607–1627, http://dx.doi.org/10.1007/s00198-020-05438-5.